1525

Microfabricated piezoelectric elastic force motor

A dissertation submitted to the Faculty of Sciences of the University of Neuchâtel, in fulfillment of the requirements for the degree of "Docteur ès Sciences"

by

Laurent Dellmann

Dipl. Microtech. Ing. EPFL

Institute of Microtechnology
University of Neuchâtel
Rue Jaquet-Droz 1, CH 2007 Neuchâtel
Switzerland

2000

IMPRIMATUR POUR LA THÈSE

Microfabricated piezoelectric elastic force motors

de M. Laurent Dellmann

UNIVERSITÉ DE NEUCHÂTEL

FACULTÉ DES SCIENCES

La Faculté des sciences de l'Université de Neuchâtel sur le rapport des membres du jury,

MM. N. de Rooij (directeur de thèse), H. Hügli, G.-A. Racine EPF Lausanne et R. Luthier EPF Lausanne

autorise l'impression de la présente thèse.

Neuchâtel, le 9 mai 2000

Le doyen:

J.-P. Derendinger

Table of contents

1. Introduction

Micromotors are suitable for low consumption, compact sizing and low temperature operation. These characteristics make them desirable for a large number of applications, such as medicine, optics, electronic devices, and watch industry, where compact, lightweight and efficient means of large angle actuation are necessary.

Motors with micro Newton scale torques and dimensions in the millimeter range cannot be easily produced with classical precision machining. An integrated and microfabricated approach, combined with classic machining techniques, make possible the realization of complex, reproducible products.

The piezoelectric motor is not actuated by an electromagnetic force but by an ultrasonic vibration. The mechanical oscillations are generated by piezoelectric elements driven by an alternating voltage. These structures used at their resonance frequencies can yield significant vibration amplitudes of a few microns in magnitude.

Many types of piezoelectric motors have been developed and some of them have already been industrialized. Section 1.2 describes some of these typical piezo-motors and their applications. The elastic force motor (EFM) is a particular type of piezo-motor and is introduced in section 1.3. The goal of this thesis was to fabricate the EFM entirely using microfabrication technologies. A partially microfabricated first prototype of the EFM, reported in 1993 and described in section 1.3.3, was the starting point of this work.

1.1. Advantages of piezoelectric motors

When the motor size is reduced, piezoelectric motors have several advantages compared to other types of motors based on electromagnetic or electrostatic actuation. In the micro-world, electrostatic motors are preferred over electromagnetic motors, because electrostatic forces scale favorably as dimensions shrink, and because dielectric materials are more easily patterned and processed than magnetic materials. The three dimensional coils required for miniaturized electromagnetic motors are much more difficult to fabricate than the small gap required for electrostatic motors. Electrostatic micro-motors have shown a certain potential [1], but also limitations [2], such as friction between the rotor and the stator, fabrication aspect ratio constraints, low torque and high voltage excitation. Many of these limitations can be avoided with the piezoelectric motors. Their main advantages are summarized in the following list.

- High power density.
- Low voltages: no air-gap is needed; mechanical forces are generated by applying a voltage across the piezoelectric film. A few microns film permits the establishment of intense electric fields with low voltages, compared to hundreds of volts needed in air-gap electrostatic motors.
- Geardown: No gearbox is necessary with piezoelectric motors, because of their ability of producing high torque at low speed.
- Holding torque: piezoelectric motors can maintain holding torque, due to friction coupling, even in absence of applied power. This propriety is very useful for a battery operated system.
- Low-noise operation.
- Low sensitivity and no generation of electromagnetic interference.

1.2. Piezoelectric motor classification [3,4,5,6]

1.2.1. Traveling wave

This type of motor already industrialized is at this time the most technologically advanced. A flexion traveling wave is obtained by the superposition of two standing waves correctly phase shifted in time ($\pi/2$) and space ($\lambda/4$), produced by two sets of piezoceramics. When the traveling wave crosses the stator, each points of the stator surface passe successively by the positions a-b-c-d-a (Fig. 1.1). Resulting in an elliptical movement going in the reverse direction than the traveling wave.

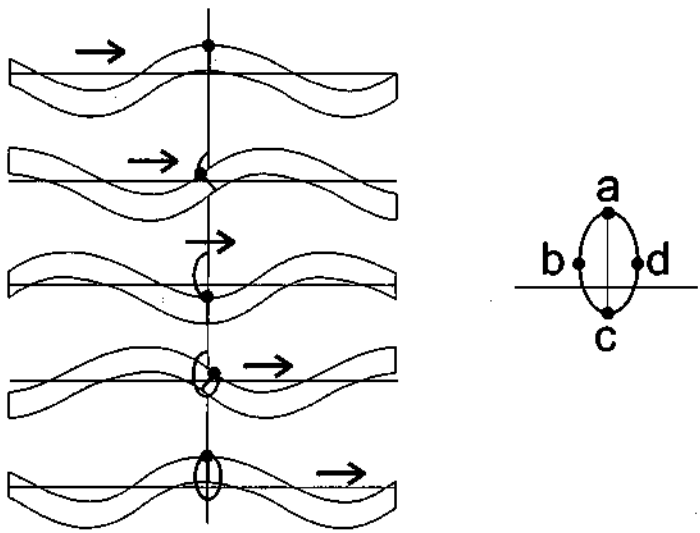

Fig. 1.1: Rotation of the cross-section when crossed by a traveling wave.

The traveling wave amplitude is maximum when the electrical excitation frequency corresponds to the mechanical resonance of the stator. The rotation direction can be changed by changing the phase shift between the two power supplies. A mobile piece (the rotor) is pressed on the top of the traveling waves so that it moves in a direction opposite to the traveling wave. When the

piezoelectric elements are placed on a circular elastic piece, a turning wave can be obtained and by the way a rotating type motor (Fig. 1.2-left). In 1987, Canon Co Ltd. produced the first ultrasonic-motor-driven autofocus lens [7], this was also the first practical application of the ultrasonic motor (Fig. 1.2-right).

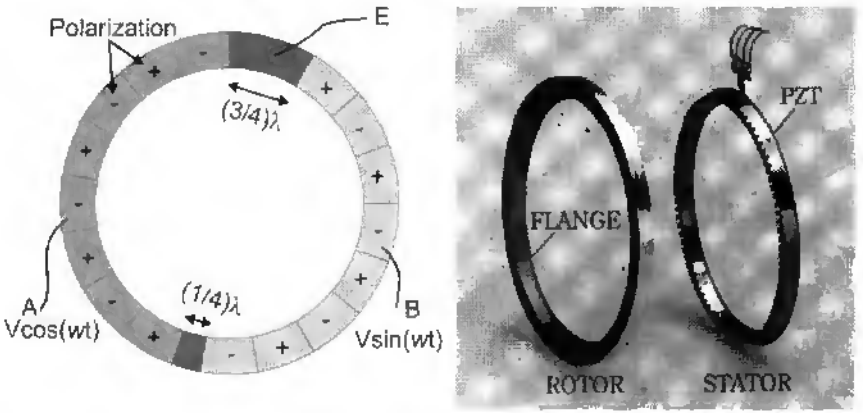

Fig. 1.2: Disposition of piezoelectric elements on the stator (left) and a Canon motor developed for the lens drive of a single-lens reflex camera [8] (right).

An elliptic motion, can also be produced by superposition of other vibration modes.

1.2.2. Mode conversion ultrasonic motors (standing wave motors)

These motors use a mode conversion to obtain two vibration modes with a single piezoelectric element. The biggest advantage of this type of motors is that the principle is very simple and so it present a great opportunity for the miniaturization. Unfortunately, only one direction of rotation is available. Several devices can be found:

- The Kumada motor [9] (Fig. 1.3). The longitudinal vibration excites a flexion mode in the coupler which is converted into a torsion mode in

the beam. The rotor, pressed onto the beam surface, is then put into motion.

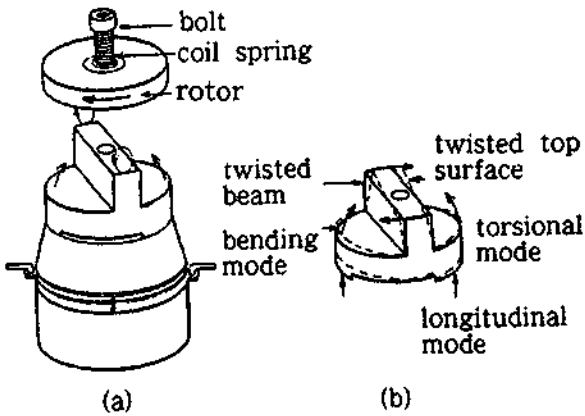

Fig. 1.3: Kumada's motor using a single resonance-mode vibrator.

- The elastic fin rotor [10] (Fig. 1.4). The key feature of this motor is its mechanism which converts the ultrasonic vibration to the movement of the rotor. The motor employs elastic fins in the rotor as the conversion mechanism, while the stator vibrates in the direction perpendicular to the movement of the rotor. The Elastic Force Motor is based on this principle and is explained in details in chapter 1.3.

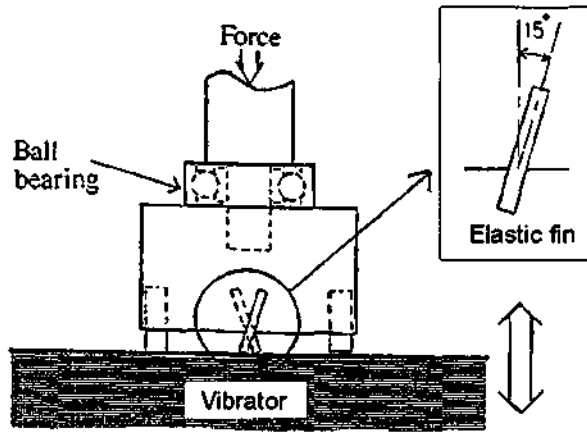

Fig. 1.4: The structure of the elastic fin motor.

1.3. The Elastic Force Motor (EFM)

1.3.1. Principles

The Elastic Force Motor (EFM) [Patents 11,12] is a standing wave type motor (chapter 1.2.1) and is based on the conversion of standing flexure waves of a piezoelectric activated resonator into an angular motion. The conversion is obtained by a mechanical rectifier analog to the Elastic Fin Rotor [10]. As described in Fig. 1.5, elastic tilted legs attached to the rotor bend elastically in the upward phase of the ultrasonic wave and relax in the downward phase. With a proper choice of tilt angle θ and friction coefficient μ, the contact point of the legs moves perpendicular to the vibrator (position 1-3 in Fig. 1.5) in the upward phase, and slides on a curved trajectory in the downward phase (position 4-6).

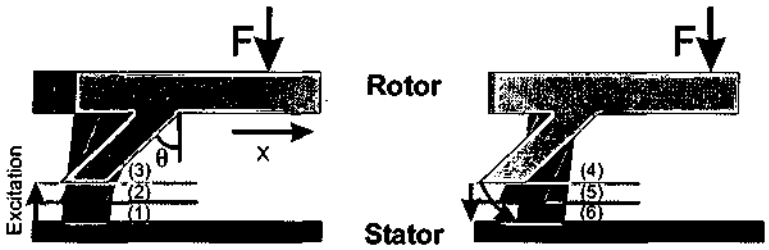

Fig. 1.5: Principle of the Elastic Force Motor (EFM). Upward (left) and downward (right) phase of operation.

The asymmetrical movement of the contact point with respect to the vibrator results in a horizontal displacement of the movable element in the X direction. The efficiency for the conversion of the electromechanical energy stored in the vibrator to the mechanical energy of the rotor is a function of geometry, tilt angle θ, elastic properties of the rotor material, loading force F and friction coefficient μ at the contact point.

1.3.2. Dynamics of the elastic force mode converter

The behavior of the elastic force mode converters (Fig. 1.5) is quite complex and not totally understood yet. A simulation of the idealized fin motor converter (Fig. 1.4) has been proposed by Kurosawa [13], using an electromechanical equivalent circuit and time integration of transient behavior. This model has revealed different operational regimes depending on the stator vibration velocity, as sketched in Fig. 1.6.

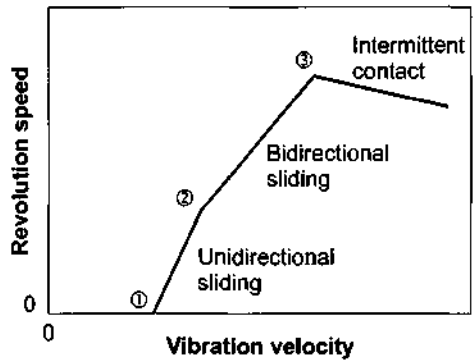

Fig. 1.6: The three operational regimes of the elastic fin motor.

The points of intersection correspond to the transition between the following regimes:

1. Continuous sticking to unidirectional sliding with permanent contact, defines a vibration velocity threshold V_{th} for non-zero revolution speed.
2. Unidirectional sliding to bi-directional sliding with permanent contact.
3. Permanent to intermittent contact. The rotor velocity is maximum.

1.3.3. The first prototype of the EFM

1.3.3.1 Motor design:

The first EFM motor was fabricated using silicon micromachining and metal micromechanical components [14]. It consisted of a silicon micromachined stator with a zinc oxide (ZnO) piezoelectric layer, and an elastic rotor fixed to a steel axis centered and preloaded by the jewel bearing of the centering wheel (Fig. 1.7).

Fabrication by micromachining offers many advantages. The batch silicon micromachining of the stator membranes combined with precise patterning of the active layer allows excellent control of wave modes. Stepping mode and

synchronous rotation can be controlled with a specific IC, combined with piezoelectric position detectors added to the membrane [15,16].

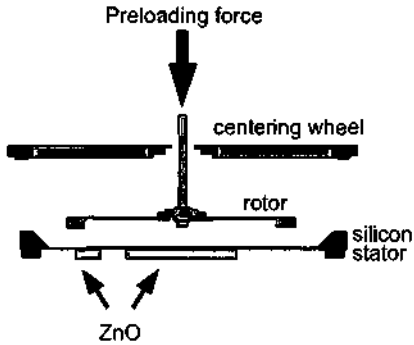

Fig. 1.7: Schematic view of the hybrid EFM motor assembly.

The silicon membrane of the stator is clamped at its border and is excited with the B_{10} mode (Fig. 1.8). The maximum deflection occurs at distance about 2/3 that of the clamping radius, and corresponds to the circle defined by the contact points of the rotor.

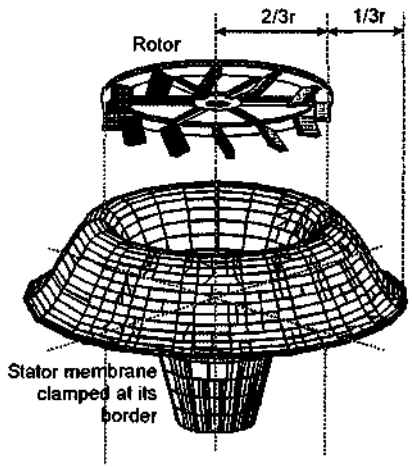

Fig. 1.8: B_{10} disk mode shape of the stator membrane with its maximum vibration amplitude corresponding to the rotor contact points.

1.3.3.2 *Fabrication:*

The fabrication process (Fig. 1.9) of the micromachined stator used five masks. Starting with <100> oriented silicon wafers, a low stress silicon nitride layer was deposited and patterned (step a). In step b, the first level of aluminum electrodes was patterned and covered by a thin CVD silicon dioxide layer (100nm). Zinc oxide was sputtered (4.5 µm thick) and structured by wet etching. A second CVD silicon dioxide layer was deposited as a passivation layer (step c) and the second electrode level was defined by a lift-off step (step d). Contact pads were opened in the last step and the stator membrane (step e) was defined by an anisotropic etch (KOH) of the cavity, using a mechanical chuck to protect the piezoelectric elements from KOH.

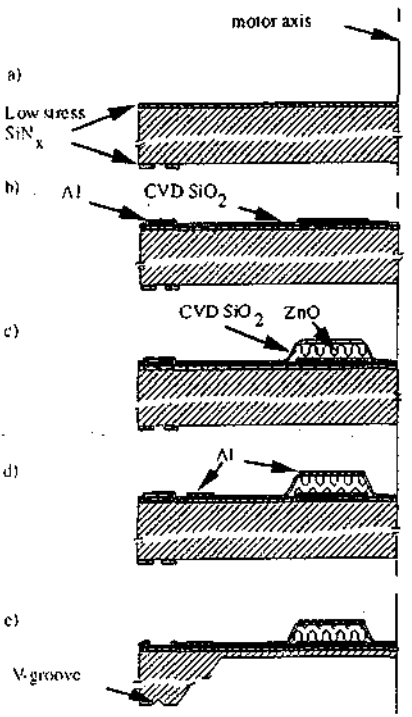

Fig. 1.9: Process overview of the micromachined stator fabrication.

The rotor (Fig. 1.10-left) was cut out of a metal foil using a laser. The legs of the rotor (Fig. 1.10-right) were folded manually to the desired tilt angle. The rotor with a diameter of 3.5 mm and a thickness of 30 µm was glued on a steel axle.

Fig. 1.10: Bottom and side views of a laser cut rotor.

1.3.3.3 Stator response

The stator response has been analyzed by means of a commercial heterodyne interferometer (Polytec) coupled with a lock-in amplifier. Mechanical resonances were measured using an XY table to scan the membrane area. Assuming a harmonic response, the deflection of the free stator is given by $A = v/2\pi f$, where v is the measured velocity and f the excitation frequency.

Fig. 1.11 shows a measurement for a 5 µm thick ZnO film on a 19 µm thick silicon membrane, with an electrical excitation of 100 mV. Data are normalized to the unit excitation voltage. The B_{10} mode which is of interest for the motor application, corresponds to the peak at 31 kHz.

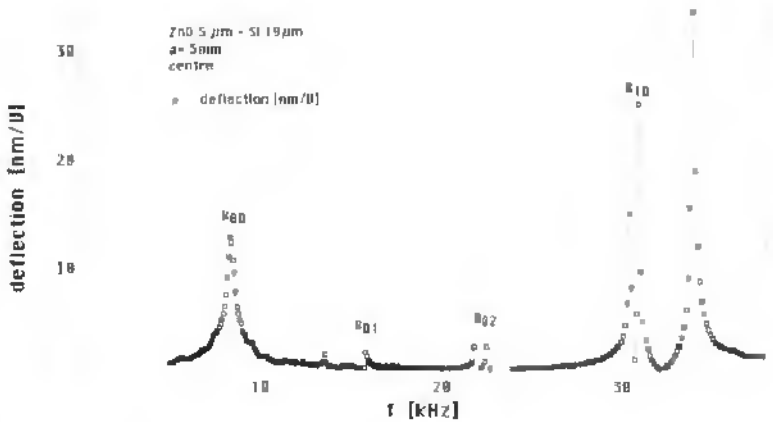

Fig. 1.11: Deflection of the membrane as a function of the AC excitation (100 mV amplitude).

1.3.3.4 Speed – Torque measurement

The complete motor mounted on a printed circuit board is shown in Fig. 1.12. The rotor was glued on an axle and centered with a bearing wheel.

Fig. 1.12: Photograph of an assembled motor mounted on a printed circuit board. The rotor can be seen under the bearing wheel.

The revolution speed was determined by measuring the rotation angle, φ, as a function of time (= dφ/dt) for different preloading force and rotor inertial mass. The torque, T, is proportional to the angular acceleration, and can be calculated assuming a known inertial load, J, (calculated from the geometry and mass density of the load).

$$T = J\frac{d\Omega}{dt} = J\frac{d^2\varphi}{dt^2}$$

Fig. 1.13 shows the transient speed and dynamic torque of the ZnO motor near the B_{10} resonance for a large load of 9.81 mN. The steady state speed was reached after about 1 s with a 10.6 V_{rms} voltage excitation. The speed increased linearly with the applied AC voltage as shown in Fig. 1.14. The maximum dynamic output torque as a function of the preloading force F_c is presented in Fig. 1.15, and shows a linear dependence followed by saturation and fall-off. The drop of the dynamic torque was due to over damping of the vibrator by a too large preloading force.

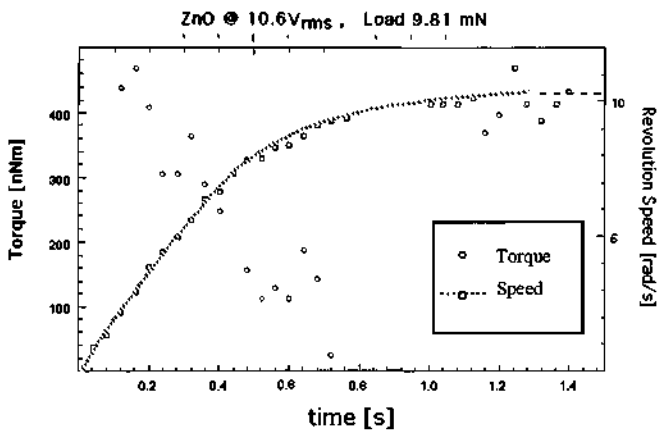

Fig. 1.13: Transient speed and dynamic torque of the ZnO motor.

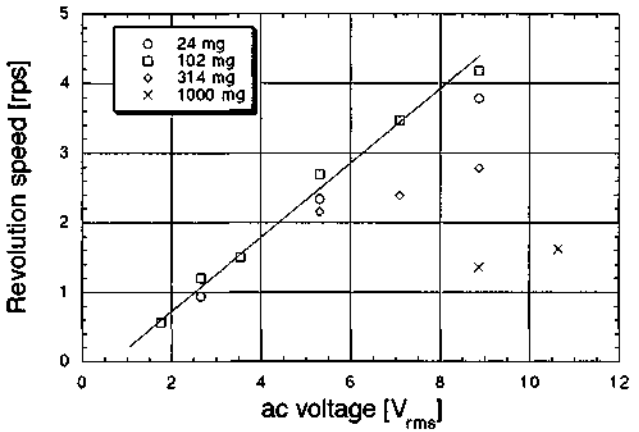

Fig. 1.14: Revolution speed as a function of applied AC voltage (the solid line is a fit for the 102 mg data).

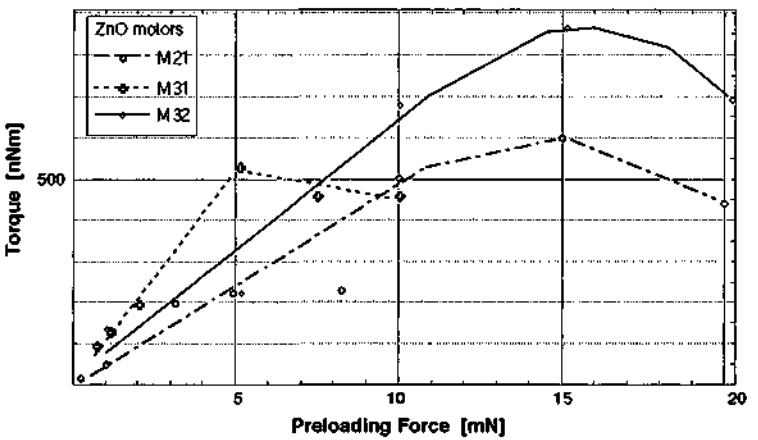

Fig. 1.15: Saturation torque as a function of preloading force F_c for three different motors.

1.3.3.5 Micromachined stator with a PZT piezoelectric layer

Several studies were done on an EFM stator with a PZT ($PbZr_xTi_{1-x}O_3$) piezoelectric layer [17], which allowed a larger piezoelectric effect to be obtained. However, PZT thin film processing and integration issues complicate device fabrication. The high deposition or annealing temperature in oxygen, and the high reactivity of the lead with silicon, requires growth of PZT on an inert bottom electrode that covers the wbole wafer. Usually, PZT is grown on a platinum bottom electrode on top of an buffer layer like SiO_2 or Si_3N_4.

Two different approaches were investigated. In the first, the ground electrode, as well as the piezoelectric film, covered the whole membrane [18]. The top electrode had an appropriate pattern to excite the useful mode. A top-to-bottom patterning process was applied in the second approach, after deposition of ground electrode, piezoelectric film and passivation layers [19].

Free membrane performance of a 0.6 μm PZT is 6 to 10 times higher than for a 5 μm thick ZnO layer. For equal revolution speed, the required voltage in PZT motors is reduced by a factor of 3 to 5. In spite of these promising results, the lifetime of sol-gel thin PZT layers is very poor compared to ZnO layers, and complicates the fabrication process and the characterization of the device severely.

1.4. Conclusions

The many advantages of the piezoelectric motors (high power density, low voltages, holding torque and low noise operation) motivated the development of the first bybrid generation of the Elastic Force Motor (EFM) with microfabrication technologies. Only the stator with a ZnO piezoelectric layer was microfabricated, while the rotor was realized with standard fabrication

technologies. The prototype showed very promising behavior with a maximum torque of 0.5 μNm at a voltage excitation of 10 V.

However many improvements need to be implemented, to obtain a micromotor compatible with industrial production. The rotor must be made with microfabrication technologies, to increase reproducibility. The size of the stator chip has to be decreased and the ratio (vibration amplitude of the stator / applied voltage) improved to satisfy the criteria for wristwatch applications. These various aspects will be considered in the following chapters.

1.5. References

1. L.-S. Fan, Y.-C. Tai and R. S. Muller, "IC-processes Electrostatic Micromotors", Sensors and Actuators, 20 (1989), pp. 41-47, 1989.
2. A. M. Flyn, L. S. Tavrow, S. F. Bart, R. A. Books, D. J. Ehrlich, K. R. Udayakumar, and L. E. Cross, "Piezoelectric Micromotor for Microrobots", Journal of Microelectromechanical Systems, Vol 1., No. 1, March 1992.
3. R. Briot, M. M. Guillemot-Amadei, A. Pelourson and C. Garabedian, "Generators for piezoelectric motors", Meas. Sci. Technol., pp. 938-946, 1993.
4. P. Gonnard, L. Eyraud and M. M. Guillemot, "Matériaux piézoélectriques pour moteurs ultrasonores, performances requises et problèmes technologiques", J. Phys. III France 4, pp 1205-1218, 1994.
5. N. W. Hagood and A. J. McFarland, "Modeling of Piezoelectric Rotary Ultrasonic Motor", IEEE Transactions on ultrasonics, ferroelectrics, and frequency control, vol. 42, No. 2, pp. 210-224, March 1995.
6. J. Wallaschek, "Piezoelectric Ultrasonic Motors", Journal of intelligent material systems and structures, Vol. 6, pp. 71-83, January 1995.
7. S. Ueha and Y. Tomikawa, "Ultrasonic Motors – Theory and Applications", Clarendon Press, Oxford, pp.198-202, 1993.
8. S. Ueha and Y. Tomikawa, "Ultrasonic Motors – Theory and Applications", Clarendon Press, Oxford, p. 54, 1993.
9. A. Kumada, "A piezoelectric ultrasonic motor, Jpn J. App. Phys. 24, Suppl. 24-2, pp. 739-740, 1985.
10. T. Uchiki, T. Nakazawa, K. Nakamura, M. Kurozawa and S. Ueha, "Ultrasonic Motor Utilizing Elastic Fin Rotor", Japanese Journal of Applied Physics, Vol. 30, pp. 2289-2291: Sep. 1991

11. Switzerland Patent N°02 553/91-0, Aug. 30 1991

12. US Patent N° 07/759 561, Sep. 13 1991

13. M. Kurozawa, T. Uchici, H. Hanada, K. Nakamura and S. Ueha, "Simulation and experimental study on elastic fin ultrasonic motor", Proc. IEEE Ultrasonics Symp., Tuscon, USA, pp. 893-896, 1992.

14. G.-A. Racine, R. Luthier and N.F. de Rooij, "Hybrid Ultrasonic Micromachined Motors", Proc. IEEE Micro Electro Mechanical Systems, Fort Lauderdale, USA, pp. 128-132, 1993.

15. G.-A. Racine, R. Luthier and N.F. de Rooij, "Piezoelectric position sensor for ultrasonic EFM motors", Sensors and Actuators A, Vol. 41-42, pp. 661-665, 1994.

16. G.-A. Racine, C. Beuret, R. Luthier, N.F. de Rooij, "Speed Control of Elastic Force Motors by Means of Integrated Piezoelectric Sensors", Proc. IEEE MEMS'94, Oiso, Japan, pp. 124-129, 1994.

17. G.-A. Racine, P. Muralt et M.-A. Dubois, "Flexural-standing-wave elastic force motor using ZnO and PZT thin Film on micromachined silicon membranes for wristwatch applications", Smart Materials Structure, vol. 7, pp. 404-416, 1998.

18. P. Muralt, M. Kohli, T. Maeder, A. Kholkin, K. G. Brooks, N. Setter and R. Luthier, "Fabrication and characterization of PZT thin film vibrators for micromotors", Sensors and Actuators A, Vol. 42, pp. 661-665, 1995.

19. G. Racine, R. Luthier, P. Luginbuhl, K. Brooks, N. Setter, N.F. de Rooij, "Hybrid Ultrasonic Elastic Force Motors Micromachined in Silicon", Integrated Ferroelectrics, 8, Vol. 1-2, pp.25-34, 1995

2. The stator

2.1. Introduction

Two types of stator have been fabricated, based on the Elastic Force Motor (EFM) principle described in chapter 1. The first one consists of a bulk PZT piezoelectric disk glued onto a copper beryllium (CuBe) membrane (Section 2.2). The second example was microfabricated entirely on silicon, with a zinc oxide piezoelectric layer (Section 2.3).

2.2. The glued CuBe / PZT stator

The stator CuBe / PZT is not microfabricated and consists of a commercially available bulk PXE PZT piezoelectric disk [1,2] glued onto a chemically etched copper beryllium (CuBe) membrane. The assembled stator membrane is fixed on a support and has an axle at its center. This type of stator was used for testing and characterizing the rotors, because of its robustness and simplicity of use.

2.2.1. Fabrication

The CuBe membrane (5 mm in diameter) was fabricated in a 100 µm thick CuBe foil by photolithography, followed by chemical etching. A hole was mecbanically drilled in the 200 µm thick PXE piezo disk, which is then glued with a conducting epoxy on the CuBe membrane. The assembled stator

membrane is then centered by the 220 µm in diameter axle and glued to the support (Fig. 2.1).

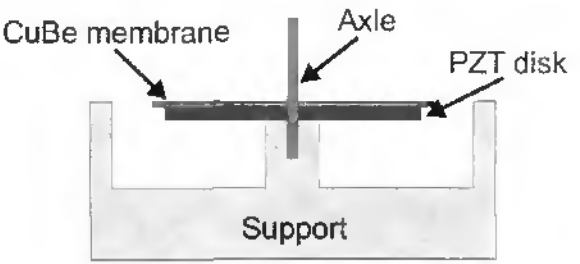

Fig. 2.1: Schematic view of the glued CuBe-PZT stator.

The main advantage of this stator over the microfabricated one was its simplicity of use. The rotor could easily be placed on the axle (Fig. 2.2) and replaced by another one without breaking the stator membrane.

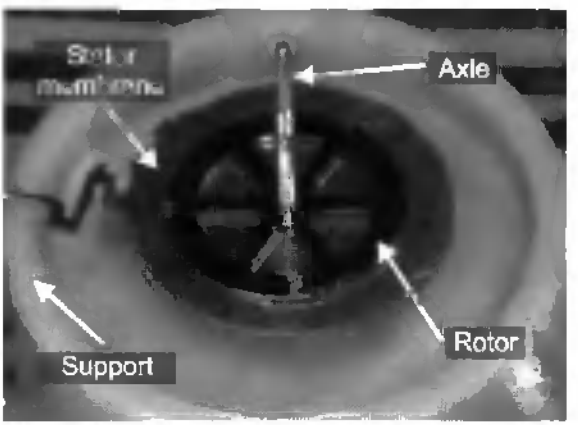

Fig. 2.2: Picture of the glued CuBe-PZT stator with a rotor centered by the axle.

The working frequency of this stator for the EFM was 38 kHz, which corresponds to the first mode of vibration (Fig. 2.3). The main peak of the

spectrum (about 500 kHz) corresponds to the resonance frequency of the PZT disk, and explains the huge amplitude of the peak at 500 kHz.

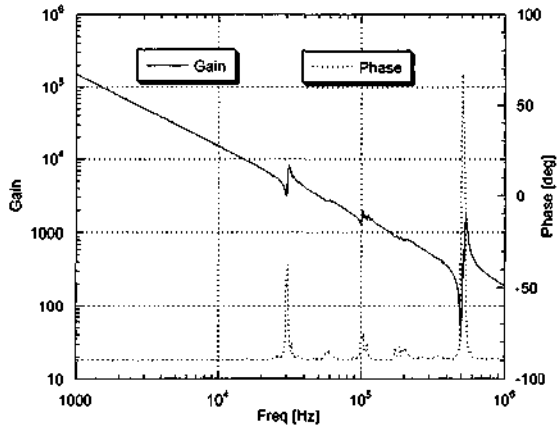

Fig. 2.3: Electrical resonances of the stator.

This easy-to-fabricate stator had large dimensions (8 mm in diameter and 3 mm in thickness). The relative crude technology used, prevents the incorporation of rotor movement detectors on the stator membrane, making the control of the stepping mode and synchronous rotation impossible.

2.3. The microfabricated silicon / ZnO stator

2.3.1. Introduction

The microfabricated silicon stator consisted of a circular membrane anchored in the center and electrically connected by springs to the substrate (Fig. 2.4). This new design allowed the use of the first vibration mode of the membrane, thereby increasing the mechanical amplitude of the oscillation in comparison to the earlier microfabricated stator design [3, Chapter 1].

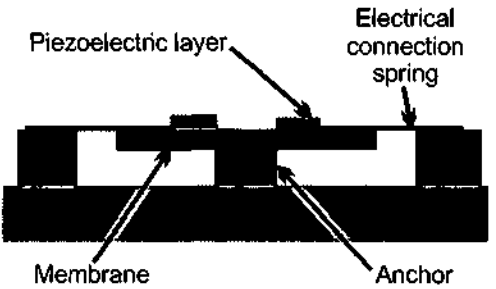

Fig. 2.4: Schematic view of the new motor design with the stator membrane clamped in the middle and the electrical connection to the substrate insured by springs.

The stator was realized entirely with microfabrication technologies, and had a silicon membrane of 3.5 mm in diameter and 20 μm thick. It was actuated with a 4 μm thick ZnO piezoelectric layer.

2.3.2. Fabrication

The fabrication process, the different layers deposition and structuring steps are described in Fig. 2.5 to Fig. 2.13 [4]. The entire ZnO process was based on the technology developed for the first generation of the microfabricated EFM [3, chapter 1].

An SOI wafer was prepared with a tensile SiO_2 layer (Fig. 2.5) to compensate for the compressive stress of the ZnO piezoelectric layer.

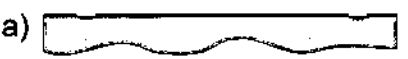

Fig. 2.5: SOI wafer prepared with a tensile SiO_2 layer.

The bottom Al electrode layer was evaporated onto the wafer and structured (Fig. 2.6). This electrode was then insulated with a thin CVD SiO_2 layer (Fig. 2.7).

Fig. 2.6: Al electrode evaporated and structured.

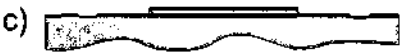

Fig. 2.7: Al electrode isolated with a thin CVD SiO_2 layer.

Zinc oxide was sputtered in a O_2/Ar partial pressure and structured by wet etching (acetic acid /phosphoric acid / DI [1:1:110]) (Fig. 2.8).

Fig. 2.8: ZnO sputtered and structured by wet etching.

A second CVD SiO_2 layer is deposited to protect the ZnO from further processing (Fig. 2.9) and the top Al electrode is evaporated and structured by wet etching (Fig. 2.10).

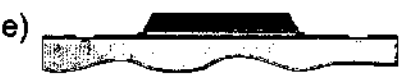

Fig. 2.9: ZnO protected by a CVD SiO_2 layer

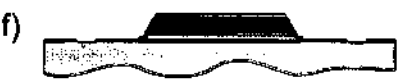

Fig. 2.10: Al electrode evaporated and structured.

The Al electrode is then protected by a PECVD silicon nitride layer (Fig. 2.11).

Fig. 2.11: Al electrode protected by a PECVD silicon nitride layer.

The geometry of the silicon membrane was defined by Deep Reactive Ion Etching (DRIE) with a 15 µm thick photoresist mask from the top surface [5] (Fig. 2.12). It was then liberated by a backside DRIE (Fig. 2.13). The thickness of the silicon stator membrane was defined by the device layer of the SOI wafer (in this case 20 µm).

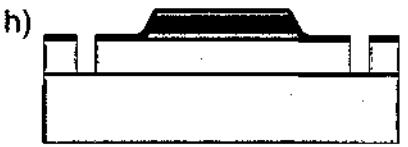

Fig. 2.12: Topside DRIE to define the silicon membrane.

Fig. 2.13: Backside DRIE to liberate the membrane.

2.3.3. Results

Freestanding membranes were obtained and successfully tested. Fig. 2.14 shows a SEM top view of the microfabricated stator with a 4 µm thick ZnO piezoelectric layer at the center of the chip. The diameter of the silicon membrane is 3.5 mm, with a thickness of 20 µm. The electrical connection of the active layer to the substrate is ensured by springs on the left and right sides of the silicon membrane. The right connection spring can be seen in Fig. 2.15,

with the detailed view of Fig. 2.16 showing the silicon spring with the aluminum layer protected by a thin CVD SiO_2 layer.

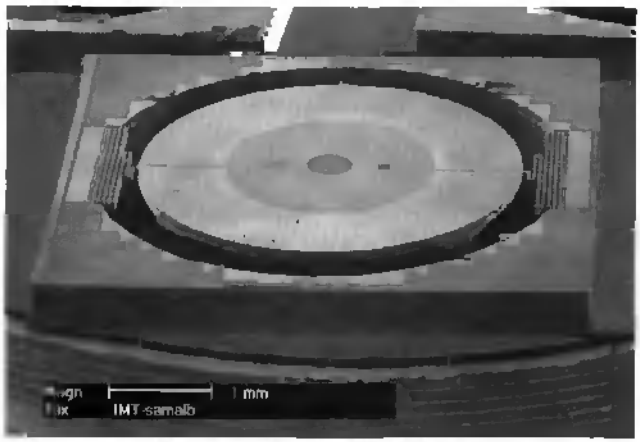

Fig. 2.14: Top view of the microfabricated silicon stator with the piezoelectric layer at the center.

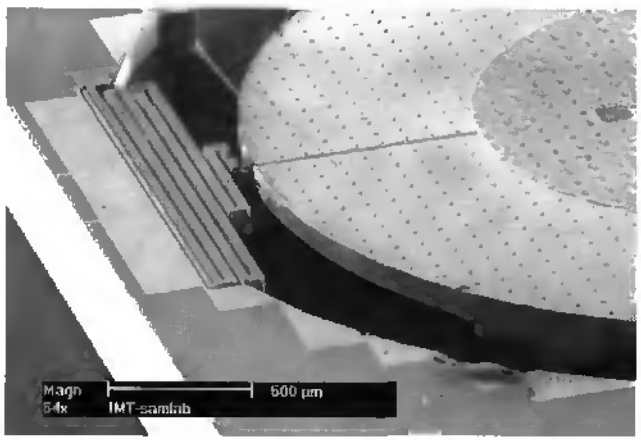

Fig. 2.15: SEM picture of a spring ensuring the electrical connection of the piezoelectric active layer to the substrate.

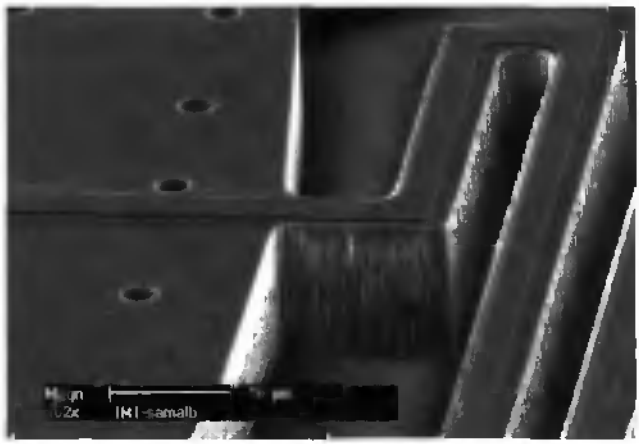

Fig. 2.16: Detailed view of the silicon spring with the aluminum layer protected by a thin CVD SiO2 layer.

The backside view (Fig. 2.17) of the chip shows the membrane anchor and the T structures used to support the membrane during the two DRIE steps. The T's were released when the oxide layer of the SOI wafer was etched. Both top and backside etches of the silicon were made with deep reactive ion etching of SOI wafers with a photoresist mask.

A procedure was developed to protect the fragile silicon membrane during the dicing. The topside of the wafer was glued on a dummy wafer with photoresist, then the backside was protected with a very thick resist layer. After the dicing, the stator chips were released in acetone.

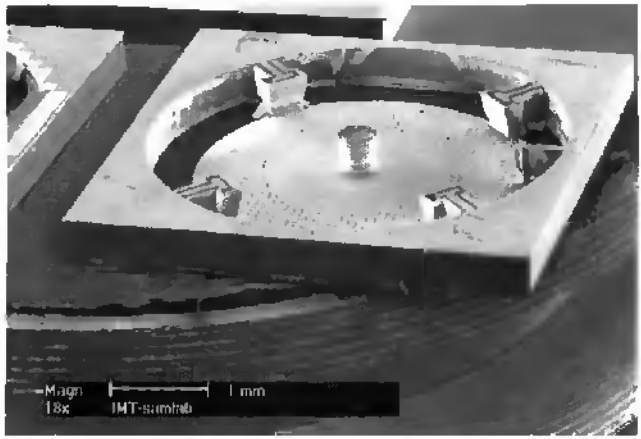

Fig. 2.17: Backside view of the microfabricated silicon stator with the anchor in the middle of the membrane and the T structures used to support the membrane during the two DRIE steps.

One of the main difficulties of this technology was the patterning of the vertical connection between the upper Al electrode and the membrane over the edge of the 4 μm ZnO layer (Fig. 2.18). During the etching of the upper Al layer, etchant seeped under the protecting photoresist mask by capillary forces and broke the Al connection. Fig. 2.19 shows a magnified view of the discontinuous Al step on the ZnO layer. This problem can be reduced by using a thicker resist mask (7 μm), or by increasing the width of the Al connection.

Another problem was the reproducibility of the ZnO sputtering process, which was very poor. Many different runs, with the same deposition parameters, yielded very different results. Even on the same wafer, huge differences in the electrical characteristics of the ZnO layer were observed. This poor quality deposition process prevented the realization of reproducible and industry-ripe devices.

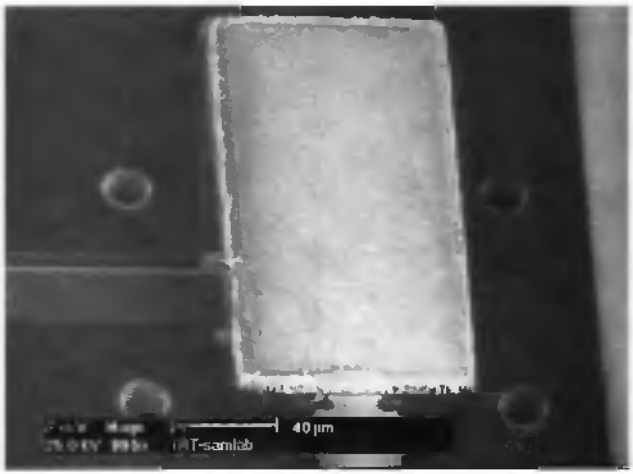

Fig. 2.18: Entire view of a detection pad with a ZnO layer between two Al electrodes. The connection to the top Al electrode is broken, due to the under-etching of the Al during the pattering of top electrode.

Fig. 2.19: Close-up view of the missing Al step on the ZnO layer.

2.3.4. Electrical and mechanical characterization of the stator

The electrical and mechanical characterization of the stator was carried out, to determine the different vibration modes of the stator membrane. The most suitable mode for motor operation could be deduced from these two types of measurements.

The free electrical resonance of the microfabricated silicon stator was measured with a gain-phase analyzer (Fig. 2.20) and exhibits two strong peaks at 12.3 and 20 kHz, respectively.

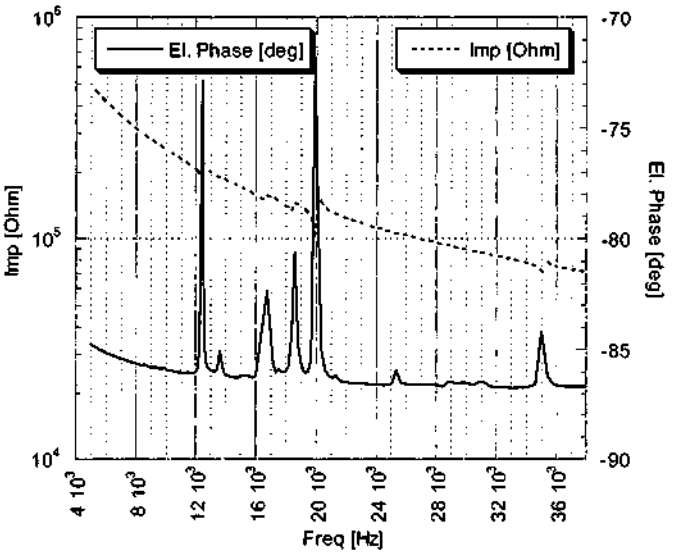

Fig. 2.20: Electrical resonance of the microfabricated silicon stator.

The free stator response was analyzed by means of a commercial heterodyne interferometer (Polytec) coupled to a lock-in amplifier. Mechanical resonances were measured using an XY table to scan the membrane area. Fig. 2.21 shows a measurement at the membrane border with an electrical excitation of 100 mV.

The interesting mode for the motor application corresponds to the peak at 20 kHz.

The deflection of the free stator is given by $A = v/2\pi f$, where v is the measured velocity and f the excitation frequency. For the 100 mV excitation, the corresponding deflection is 6 nm. Assuming that the deflection is linearly dependent on voltage excitation, the deflection for a typical excitation of 4 V would be 0.24 µm.

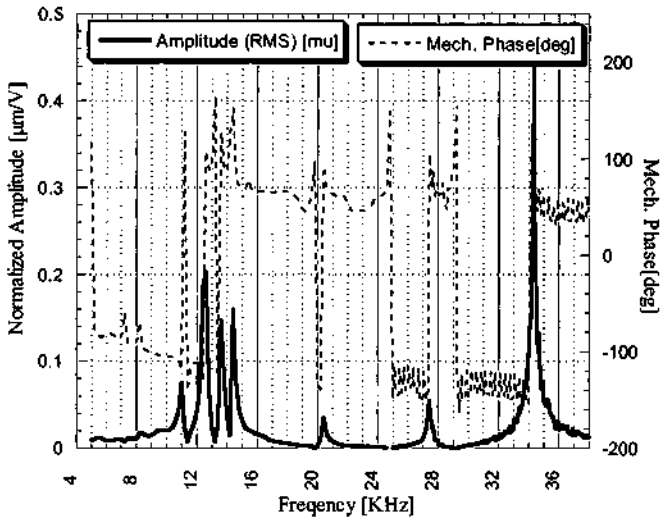

Fig. 2.21: Mechanical resonance measured with an heterodyne interferometer.

The resonance peaks amplitudes in Fig. 2.20 and Fig. 2.21 are not exactly the same. This is due to the difference between the two methods of measurement. The electrical measurement was done on the entire membrane of the stator and thereby indicates the average resonances for the entire membrane. On the other hand, the mechanical measurement was done at a precise point on the membrane, defined by the laser spot of the interferometer, and will show only the resonances present at this point.

Slight stator membrane asymmetry, as well as perturbations introduced by the two electrical connection springs, could explain the differences between the electrical and mechanical amplitude of the 20 kHz mode used for motor operation.

2.3.5. Complete motor

Fig. 2.22 shows a complete motor with a nickel rotor lying on a silicon stator without any preloading force or guiding. The bonding wires, connecting the stator chip to the PCB, can be observed near the electrical connection springs.

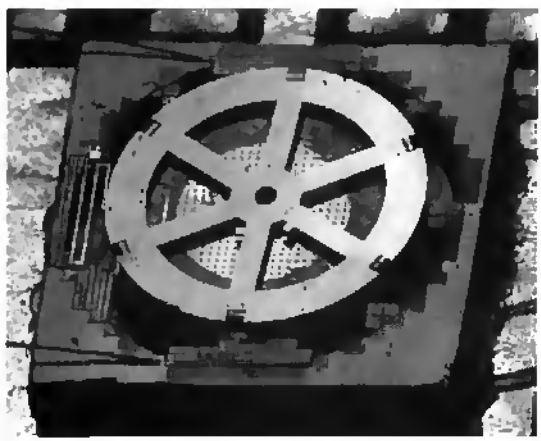

Fig. 2.22: Complete motor with a microfabricated silicon stator and a microfabricated rotor. The piezoelectric ZnO layer can be observed under the rotor.

The output torque of the EFM is directly proportional to the preloading force applied on the rotor. This can be easily explained by the fact that the rotor has to be in contact with the stator in order to assure a good conversion of the stator vibration.

A special experimental setup was developed to control the preloading force and the position of the axle in the three directions (Fig. 2.23). The axle was guided

with two jewel bearings and could be loaded at its upper end with different calibrated masses (Fig. 2.24).

Fig. 2.23: Picture of the motor test setup with micro-manipulators.

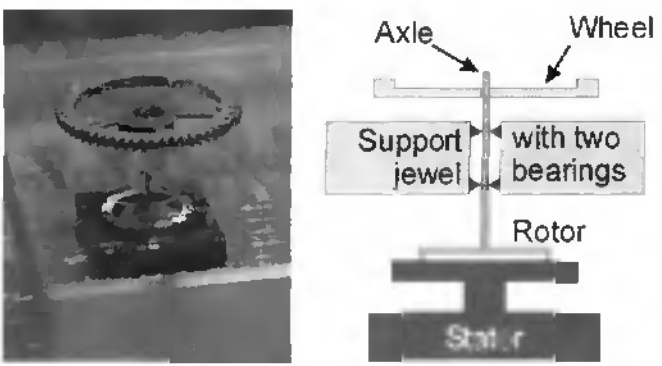

Fig. 2.24: The axle is guided with two jewel bearings. It is loaded at his upper end by a wheel and can be loaded with different calibrated masses.

The two jewel bearings induced a very high friction on the axle, preventing its rotation by the rotor. Contact between the rotor and the stator was maintained and guided by the axle without any preloading force. This led to the rotor not being in continuous contact with the stator and an irregular rotation speed. Even

at low voltage excitation, stator deflection was too high for the light, unloaded rotor. Therefore, no motor characteristics, such as speed and torque, could be extracted from this experiment. Successful motor operation was obtained from a 4 V_{RMS} sinusoidal excitation at 20 kHz. The movement of the rotor can be observed in the six consecutive video pictures of the Fig. 2.25.

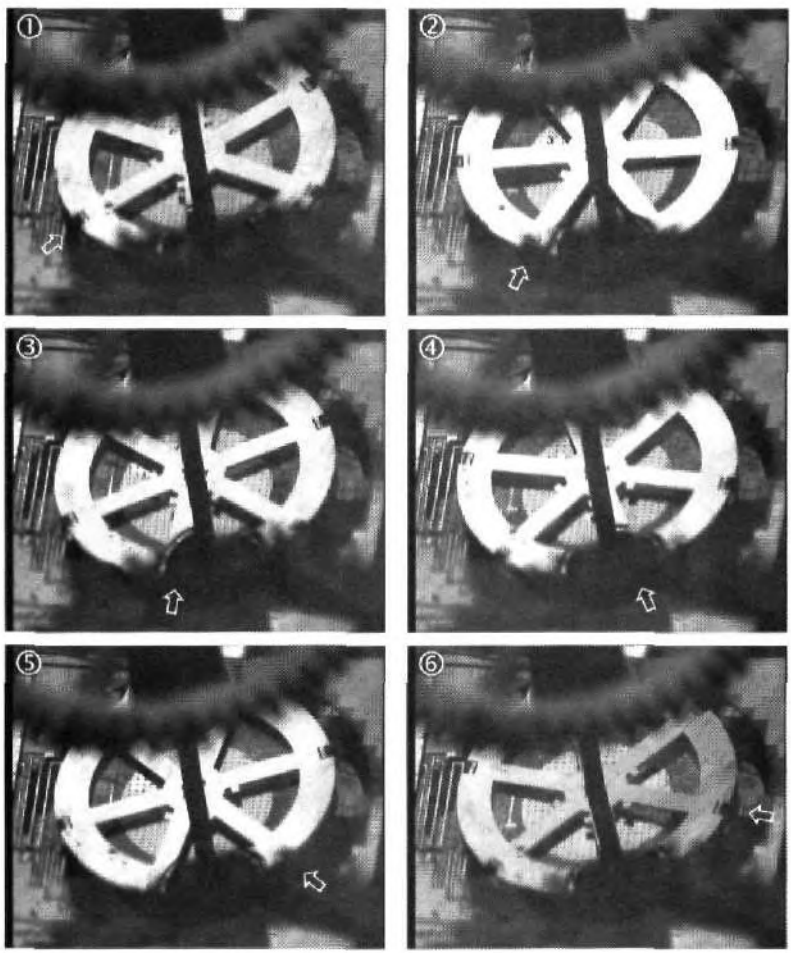

Fig. 2.25: Motor operation view during six consecutive video pictures.

This very promising behavior showed that the design of the stator clamped in its middle is more efficient than the stator membrane clamped in its border. Other measurements have to be done with calibrated loads on the rotor, to determine more precisely the motor characteristics. The principle of the axle has to be reconsidered entirely to avoid manipulation and guiding problems. The guiding and centering function of the rotor has to be insured on the stator chip with interfaces permitting the connection to the macro world. Such as a hole into the stator chip to guide the external axle or a microfabricated axle.

2.4. Conclusions

The microfabricated stator with a ZnO piezoelectric layer exhibited a good mechanical and electrical behavior. The motor operation is done at a frequency of 20 kHz and with a typical voltage excitation of 4 V. This new design, which allows the use of the first mode of vibration of the membrane, has shown increased mechanical amplitude of the oscillation, in comparison to early stator design.

The combination of the integrated ZnO piezoelectric technology and the deep reactive ion etching has permitted the realization of complex free standing structures. One of the most important problems encountered during the development of this process, was the reproducibility of the ZnO sputtering deposition. It needs to be drastically improved, to insure a controllable mechanical behavior of the stator and a better fabrication yield.

The weakness of the membrane, due to a too small thickness, prevents to realize speed and torque measurements. This problem has shown the difficulty to manipulate microfabricated structures and this has to be taken into account for the design of the next generation to improve the connection of the micromotor to the macro world.

2.5. References

1. PIEZOXIDE (PXE), Eigenschaften und Anwendungen, Valvo Philips Bauelemente, pp. 83-92, 1998
2. Ph. Luginbuhl, P.-F. Indermuhle, M.-A. Grétillat, F. Willemin, N.F. de Rooij, D. Gerber, G. Gervasio, J.-L. Vuilleumier, D. Twerenbold, M. Düggelin, R. Guggenheim, "Micromachined Injector for DNA Mass Spectrometry"; Digest of Technical Papers 10th Internat. Conf. on Solid-State Sensors and Actuators, TRANSDUCERS '99, Sendai, Japan, pp. 1130-1133, 1999
3. G.-A. Racine, R. Luthier and N.F. de Rooij, "Hybrid Ultrasonic Micromachined Motors", Proc. IEEE Micro Electro Mechanical Systems, Fort Lauderdale, USA, pp. 128-132, 1993.
4. L. Dellmann, G.-A. Racine, N.F. de Rooij, "Micromachined piezoelectric elastic force motor", Proc. IEEE Micro Electro Mechanical Systems (MEMS '00), Miyazaki, Japan, p. 52-55, 2000
5. P.-A. Clerc, L. Dellmann, F. Grétillat, M.-A. Grétillat, P.-F. Indermühle, S. Jeanneret, Ph. Luginbuhl, C. Marxer, T.L. Pfeffer, G.-A. Racine, S. Roth, U. Staufer, C. Stebler, P. Thiébaud, N.F. de Rooij, "Advanced deep reactive ion etching: a versatile tool for micromechanical systems", Journal of Micromechanics and Microengineering, vol. 8, pp. 272-278, 1998.

3. The rotor

3.1. Introduction

The function of the rotor is to convert the standing flexural waves of a piezoelectrically activated resonator into an angular motion. This conversion is mediated by inclined legs attached to the rotor.

The first version of the rotor was fabricated with laser cutting, followed by manual bending of the legs. However, this method is not appropriate for industrial production due to poor reproducibility and high price. To overcome these technical and economic constraints, it was decided to realize the rotor with micromachining techniques used in the microelectronic industry (photolithography, electrodeposition). The first approach was the development of a micromachined rotor with inclined legs. This proved to be unsuccessful, however, because the realization of reproducible inclined molds for electroplating by photolithography was very difficult. It was decided to replace the inclined rotor legs by vertical elements having the same mechanical characteristics as the laser-cut rotor.

3.2. The first generation fabricated manually

The first version of the rotor was fabricated from a 20 µm thick cooper-beryllium foil, using laser cutting followed by manual bending of the legs. With this technique, it was easy to obtain structures, but a good reproducibility was not assured. Fig. 3.1 shows a bottom view (left image) and a side view (right image) of a 12-leg rotor with a diameter of 3.2 mm. The bending angle of the legs is not constant, which can easily be explained by the manual bending method.

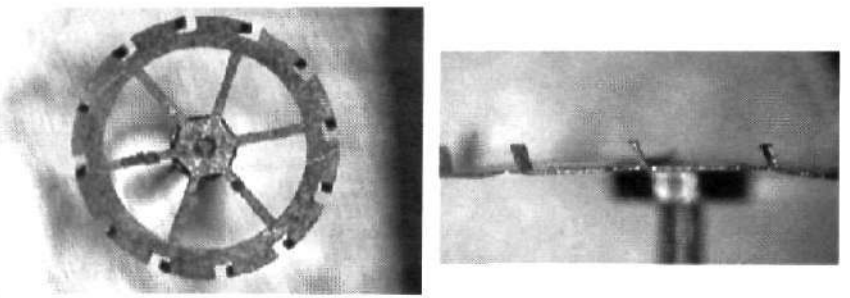

Fig. 3.1: Bottom and side views of a laser cut rotor.

3.3. The first microfabricated generation with inclined legs

In order to reduce these disadvantages, micromachining techniques used in the microelectronic industry (photolithography and electrodeposition) were investigated. The rotor wheel and inclined legs were fabricated with nickel electrodeposition in photoresist moulds [1] in work done prior to this thesis.

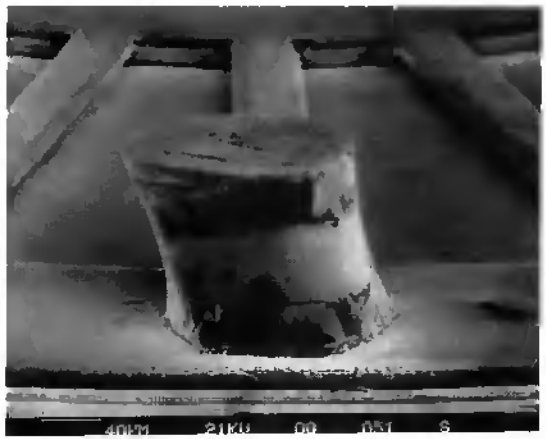

Fig. 3.2: Close-up view of a nickel microfabricated rotor with inclined nickel legs.

The reproducibility of the fabrication was very bad, due to a complex multi-layer photoresist process. Fig. 3.2 shows an inclined leg obtained with this technology.

3.4. From inclined to vertical legs

3.4.1. Concept

Since the realization of reproducible electroplated inclined structures by micromachining (Fig. 3.2) was difficult, it was decided to replace the inclined rotor legs by vertical elements (Fig. 3.3) having the same mechanical characteristics as the laser cut rotor [2].

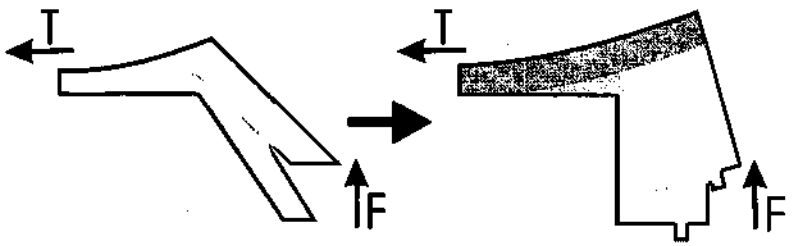

Fig. 3.3: Original inclined leg (left) compared to a new vertical leg (right).

In the original design (Fig. 3.3 left), a net average torque, T, is generated by the reaction to the vertical sinusoidal force, assuming an elastic deformation of the beam relative to the inclined leg. The same mechanical effect is obtained using a multilevel rigid body coupled to an elastic beam (Fig. 3.3 right).
In the new design, the rotor had two main parts, the wheel and the vertical legs (Fig. 3.4).

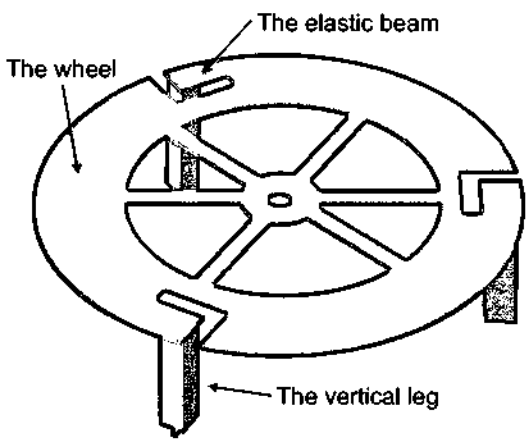

Fig. 3.4: Schematic view of the vertical leg design of the microfabricated rotor.

The wheel was realized by nickel electroplating in a photoresist mould (section 3.6) and the legs were fabricated by photostructuration of an SU-8 epoxy (section 3.7) or by nickel electroplating in a photoresist mould (section 3.8).

3.5. Design of the rotor with vertical legs

3.5.1. Principles

This new rotor design will define a nickel rotor with vertical legs having the same mechanical characteristics as the manual fabricated rotor with inclined legs.

The case of an inclined leg will be studied, because the vertical leg is a particular case of this. The leg can be broken down into two beams (Fig. 3.5), which can be then studied separately.

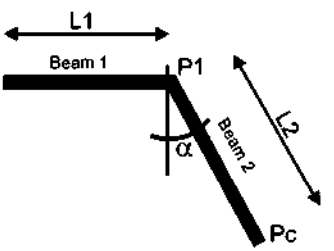

Fig. 3.5: Schematic view of the inclined leg.

The deformation of both beams will be considered when a force is applied to them to determine the compliance matrix, C, in Equation (1). This matrix describes the relationship between the applied forces in the x and y directions and the deformation. The rigidity matrix, K, in Equation (2), is the inverted compliance matrix. It gives the forces in x and y as a function of the displacements, Ux and Uy (Fig. 3.6), and allows the deformed leg to be characterized. This K matrix is interesting for the EFM motor study, because it establisbes the link between stator excitation (displacement) and the force applied by the leg on the stator.

Two matrices will be calculated, one for each beam, in order to simplify consideration of the vertical leg case. In this case the second beam is considered as not buckled, because it is much thicker than the first beam.

The force is always applied at the contact point, Pc (Fig. 3.5). Both beams are considered independently, meaning that the deformation of Beam 1 will be calculated assuming Beam 2 is not buckled, and vice versa.

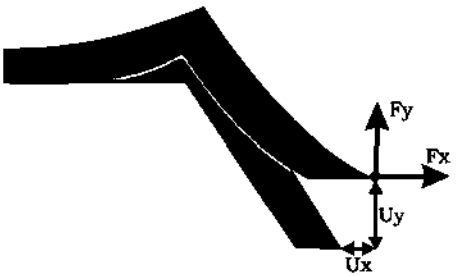

Fig. 3.6: Deformation of the leg under strain.

Compliance matrix

$$\begin{pmatrix} Ux \\ Uy \end{pmatrix} = \underbrace{\begin{pmatrix} Cxx & Cxy \\ Cyx & Cyy \end{pmatrix}}_{C} \begin{pmatrix} Fx \\ Fy \end{pmatrix} \quad (1)$$

Rigidity matrix

$$\begin{pmatrix} Fx \\ Fy \end{pmatrix} = \underbrace{\begin{pmatrix} Kxx & Kxy \\ Kyx & Kyy \end{pmatrix}}_{K = C^{-1}} \begin{pmatrix} Ux \\ Uy \end{pmatrix} \quad (2)$$

The four compliance matrix coefficients (C_{ij}) are calculated from the x and y components of the deformations and the forces.

3.5.1.1 *Compliance matrix C_1 of beam 1*

The compliance matrix coefficients (Equation (3)) are obtained by dividing calculated deformations (Equations (4) to (8), details in Appendix A) by the corresponding force.

$$\begin{pmatrix} Ux \\ Uy \end{pmatrix} = \underbrace{\begin{pmatrix} C1xx & C1xy \\ C1yx & C1yy \end{pmatrix}}_{C_1} \begin{pmatrix} Fx \\ Fy \end{pmatrix} \quad (3)$$

$$C1xx = \frac{Ux(Fx)}{Fx} \qquad C1xy = \frac{Ux(Fy)}{Fy} \tag{4}$$
$$C1yx = \frac{Uy(Fx)}{Fx} \qquad C1yy = \frac{Uy(Fy)}{Fy}$$

$$C1xx = \frac{U_x(Fx)}{Fx} = \frac{L_1 L_2^2 \cos^2(\alpha)}{EI} \tag{5}$$

$$C1xy = \frac{U_x(Fy)}{Fy} = \left(\frac{L_1 L_2 \sin(\alpha)}{EI} + \frac{L_1^2}{2EI}\right) L_2 \cos(\alpha) \tag{6}$$

$$C1yx = \frac{U_y(Fx)}{Fx} = \frac{L_1^2 L_2 \cos(\alpha)}{2EI} + \frac{L_1 L_2^2 \cos(\alpha)\sin(\alpha)}{EI} \tag{7}$$

$$C1yy = \frac{U_y(Fy)}{Fy} = \frac{L_1^2 L_2 \sin(\alpha)}{2EI} + \frac{L_1^3}{3EI} + \left(\frac{L_1 L_2 \sin(\alpha)}{EI} + \frac{L_1^2}{2EI}\right) L_2 \sin(\alpha) \tag{8}$$

3.5.1.2 Compliance matrix C_2 of beam 2

The compliance matrix coefficients (Equation (9)) are obtained by dividing calculated deformations (Equations (10) to (13), details in Appendix A) by the corresponding force.

$$\begin{pmatrix} Ux \\ Uy \end{pmatrix} = \underbrace{\begin{pmatrix} C2xx & C2xy \\ C2yx & C2yy \end{pmatrix}}_{C_2} \begin{pmatrix} Fx \\ Fy \end{pmatrix} \tag{9}$$

$$C2xx = \frac{U_x(Fx)}{Fx} = \frac{L_2^3 \cos^2(\alpha)}{3EI} \tag{10}$$

$$C2xy = \frac{U_x(Fy)}{Fy} = \frac{L_2^3 \cos(\alpha)\sin(\alpha)}{3EI} \tag{11}$$

$$C2yx = \frac{U_y(Fx)}{Fx} = \frac{L_2^3 \cos(\alpha)\sin(\alpha)}{3EI} \tag{12}$$

$$C2yy = \frac{U_y(Fy)}{Fy} = \frac{L_2^3 \sin^2(\alpha)}{3EI} \tag{13}$$

3.5.1.3 Compliance and rigidity matrix

A. Complete compliance matrix

The complete compliance matrix (Eq. (1)) is the sum of the matrix of legs 1 and 2 (Eq. (3) and (9)).

Complete compliance matrix : (14)

$$C = \begin{pmatrix} Cxx & Cxy \\ Cyx & Cyy \end{pmatrix} = C1 + C2 = \begin{pmatrix} C1xx + C2xx & C1xy + C2xy \\ C1yx + C2yx & C1yy + C2yy \end{pmatrix}$$

B. Rigidity matrix

The rigidity matrix (Equation (2)) is obtained by inverting the compliance matrix (equation (14)).

$$K = \begin{pmatrix} Kxx & Kxy \\ Kyx & Kyy \end{pmatrix} = \frac{1}{CxxCyy - CxyCyx} \begin{pmatrix} Cyy & -Cxy \\ -Cyx & Cxx \end{pmatrix} \quad (15)$$

3.5.2. Leg behavior under stator excitation

When a leg is deformed in a random direction (expressed in terms of x and y components), it produces two perpendicular forces in the x and y directions. These two forces can be calculated using the rigidity matrix of the leg (Equation (15)).

In the case of the EFM, only the y deformation is interesting, because it corresponds to the direction of the stator excitation.

The deformation, U_y, generates a force, F, which can be expressed in terms of two perpendicular forces, Fx and Fy (Fig. 3.7). This force pair can be modeled as a pair of springs strained by the deformation, U_y. (Fig. 3.8).

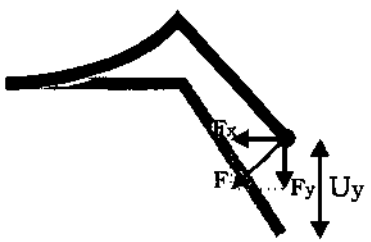

Fig. 3.7: Schematic view of the leg deformed in the y direction.

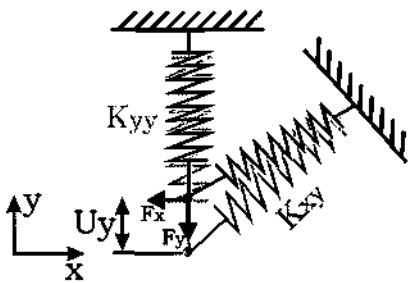

Fig. 3.8: Bidimensional mechanical model of the leg.

These considerations indicate that only the coefficients, Kyy and Kxy, are necessary to describe the legs in the case of EFM operation, and that the new rotor with vertical legs must have Kyy and Kxy identical to the CuBe laser-cut rotor.

3.5.3. *The rigidity matrix of the CuBe rotor*

The dimensions of the CuBe rotor have been measured on SEM pictures and are reported in the Table 1.

Table 1: Measured dimensions of the CuBe rotor.

Length beam 1	Length beam 2	Width	Thickness	Angle
220 µm	60 µm	120 µm	30 µm	17°

The data introduced into the Matlab program (Appendix A) gave the following rigidity matrix (Eq. (16)), with the two coefficients, Kyy and Kxy, important for the nickel leg dimensioning.

$$K = 10^5 \cdot \begin{pmatrix} 0.3310 & -0.6639 \\ -0.6639 & 1.4992 \end{pmatrix} \tag{16}$$

3.5.4. *Dimensioning of the nickel rotor with vertical legs*

The two spring constants (Kyy and Kxy) of the nickel rotor have to be identical to those of the CuBe rotor (Kyy=$1.5 \cdot 10^5$ N/m and Kxy=$6.6 \cdot 10^4$ N/m). Beam 2 is assumed to be not buckled (compliance matrix equal to zero). The equivalent angle is defined by the position of the contact point of the leg on the stator and is chosen to be equal to 7°. The thickness of Beam 1 is 20 µm. This corresponds to the same resonance frequency for the entire Ni wheel as for the entire 30 µm CuBe wheel.

The Matlab program (Appendix **A**) calculates the spring constant matrix of the nickel leg, as a function of Beam 1 and Beam 2 lengths (L1 and L2). This allows a pair of points (L1 and L2) corresponding to the identical Kyy and Kxy coefficients of the CuBe leg to be found.

Different beam widths have been taken into account for the dimensioning.

The following tables summarize the different results (Table 2, Table 3 and Table 4).

- **50 µm width beams**

Table 2: (L1, L2) pairs for 50 µm wide beams

L1 [µm]	L2 [µm]	Kyy [10^5 N/m]	Kxy [10^4 N/m]
140	***95***	***1.5***	***6.6***
100	110	0.9	7.1
60	140	0.5	6.6

- **80 µm width beams**

Table 3: (L1, L2) pairs for 80 µm wide beams

L1 [µm]	L2 [µm]	Kyy [10^5 N/m]	Kxy [10^4 N/m]
150	***110***	***1.4***	***6.4***
120	120	1.1	6.6
100	130	0.9	6.7

120 µm width beams

Table 4: (L1, L2) pairs for 120 µm wide beams

L1 [µm]	L2 [µm]	Kyy [10^5 N/m]	Kxy [10^4 N/m]
180	***120***	***1.6***	***6.6***
160	130	1.3	6.6
140	140	1.1	6.5

Three (L1, L2) pairs, shown in bold in the tables, allows the duplication of the CuBe spring constants, but only the 50 μm wide beams with L1=95 μm and L2=140 μm can be fabricated without too much difficulty. The other two have a Beam 2 length, which is too long to be easily fabricated with micromachining technologies.

Fig. 3.9 shows a schematic view of the vertical leg with the most important dimensions summarized in the Table 5.

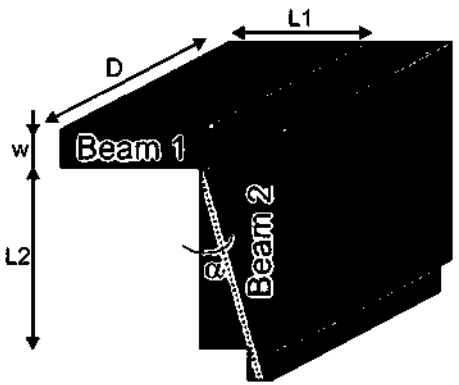

Fig. 3.9: Schematic view of the vertical leg.

Table 5: Summary of the important dimensions of the vertical leg.

Length of beam 1 (L1)	140 μm
Length of beam 2 (L2)	95 μm
Width of the beam (D)	50 μm
Thickness of the beam 1 (w)	20 μm
Equivalent angle (α)	7°

Other lengths of Beam 2 (L2) were also fabricated, to evaluate the behavior of the new rotor as a function of L2.

3.6. The wheel fabrication

The wheel was fabricated by electrodeposition of nickel into a thick photoresist mould. A silicon wafer was used as substrate with a 0.2 µm thick Ti sacrificial and seed layer. A thick positive photoresist layer [3,4] (Clarian AZ-4562 / 38 µm) was spun onto this wafer (Fig. 3.10) with a rotating cover spinner (Karl Süss RC8 Spin Coater, Germany).

Fig. 3.10: Coating of the 40 µm thick resist layer onto the Ti coated Si wafer.

This type of spinner allows the deposition of thick, uniform layers in one step by minimizing air turbulence effects. Resist accumulation on the wafer borders (edge bead) prevents a good contact between the mask and the resist layer. This can be reduced to 2-3 mm for a 3" wafer, by introducing huge, but very brief accelerations during the spinning process. The prebake is one of the most critical steps, because of its direct influence on illumination energy, development time, structure resolution and mold walls [5]. The prebake is realized with a ramped hotplate. To improve the resist adhesion, a ramp (40°C to 90°C in 10 min) is used, before the temperature plateau of 90°C for 60 min. The illumination is realized with a mask aligner (Electronic Vision AL6-2, Austria) with mercury lamp (355nm, 405nm and 436nm) in vacuum contact mode, to improve structure definition by reducing diffraction effects (Fig. 3.11).

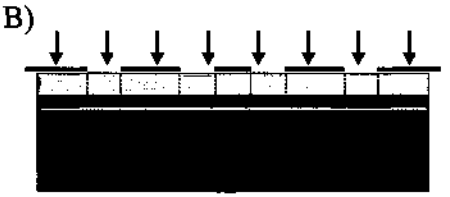

Fig. 3.11: Exposure of the resist layer

The humidity has to be very constant to ensure good reproducibility. During development with AZ-400K [1:4] (1 AZ-400K part for 4 parts DI water), the wafer was energetically agitated in the bath, enhancing developer penetration in the small mold structures (Fig. 3.12).

Fig. 3.12: Development of the resist layer

To avoid distortion of photoresist patterns, no postbake was done [6]. The resist mould was then treated in HCl to clean the seed layer surface.

Fig. 3.13: A 38 µm thick photoresist mould of the wheel, before the nickel electrodeposition.

The mould (Fig. 3.13) was now ready for the 20 µm thick electrodeposition (Fig. 3.14) in a commercial Nickel Sulfamate-type bath, followed by stripping of the resist mould (Fig. 3.15).

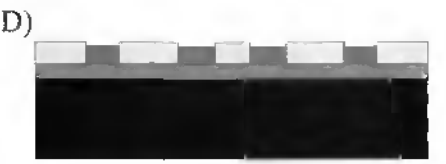

Fig. 3.14: Electroplating the nickel in the resist mould.

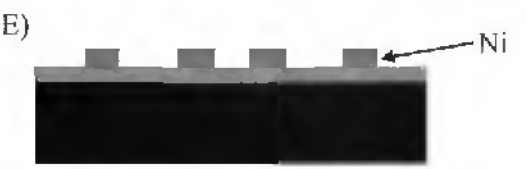

Fig. 3.15: Stripping of the resist mould.

The wheel fabrication process was terminated and was followed by fabrication of the legs, which can be achieved in two different ways, either by SU-8 structuring or nickel electrodeposition in a 100 µm thick photoresist mould. These two processes are described in the two following sections.

3.7. The SU-8 legs

The first method for fabricating the vertical legs involved the patterning of vertical sidewall structures in SU-8 (one or two levels). The SU-8 technology is very powerful and easy to use, and structures up to 500 µm can be realized with a standard photolithography equipment [7,8,9]. SU-8 is a negative tone resist and makes possible the realization of two-level structures.
The SU-8 layer was directly spun on the electrodeposited nickel wheel (Fig. 3.16) using a conventional spin coater (Fig. 3.17). No surface pretreatment, such as priming or oxygen plasma, were performed.

Fig. 3.16: Electrodeposited nickel wheel.

Fig. 3.17: SU-8 layer directly spun on the electrodeposited nickel wheel.

The substrate was then prebaked on a ramped hotplate, with a ramp (40°C to 95°C / 8 min) and a plateau at 95°C for 12 min. The illumination (mask 1) was realized with an Electronic Vision AL6-2 mask aligner in proximity mode (Fig. 3.18).

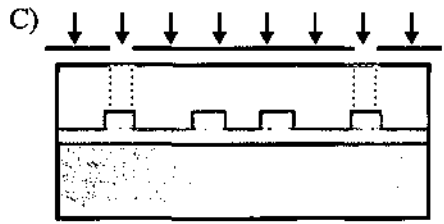

Fig. 3.18: UV illumination of the legs SU-8 layer.

Before the postbake, the resist was kept in air for 30 min to improve crosslinking of the exposed regions. Then the postbake was performed on the hotplate with the same parameters as for the prebake.

A second, 15µm thick SU-8 layer was then directly spun and prebaked in an oven at 90°C during 5 min. The oven prebake heats preferentially the upper SU-8 layer and prevents overtreatment for the lower SU-8 layer. The prebake is then followed by UV illumination (mask 2) (Fig. 3.19) and another oven postbake to perform the crosslinking of SU-8.

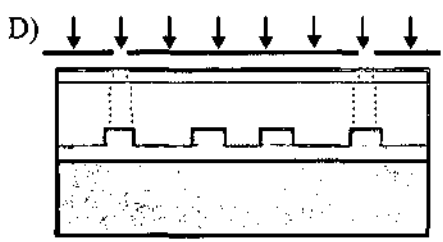

Fig. 3.19 UV illumination of the second SU-8 layer.

Levels 2 and 3 were simultaneously developed in PGMEA (propylenglycol-monomethylether-acetate) (Fig. 3.20).

Fig. 3.20: Both SU-8 layers simultaneously developed in PGMEA.

Finally the wafer was rinsed with isopropanol and hardbaked at 200°C for 30 min in an oven. In the final step the fabricated structures were released by a sacrificial etch of the Ti in a hydrofluoric acid (HF) solution (Fig. 3.21). SU-8 / nickel structures survived more than 40 min in HF.

Fig. 3.21: Structures released by sacrificial etch of the Ti layer in HF.

Fig. 3.22 shows a nickel wheel with three SU-8 vertical legs. The thickness of the nickel layer is 20 µm

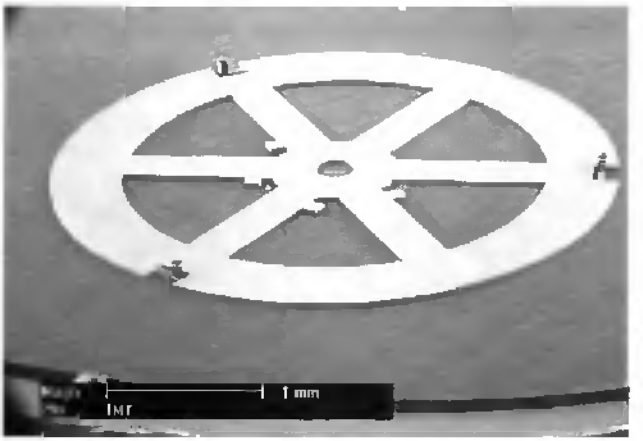

Fig. 3.22: SEM picture of a rotor with three SU-8 legs

Fig. 3.23 shows a detail of a Ni wheel surmounted by a two-level SU-8 vertical leg. Here the aspect ratio of the leg body is 2, but values up to 10 have been obtained in test structures. The dimensions of the first SU-8 level and of the contact point are 95 x 50x 50 µm and 15 x 10 x 20 µm (height x width x length), respectively.

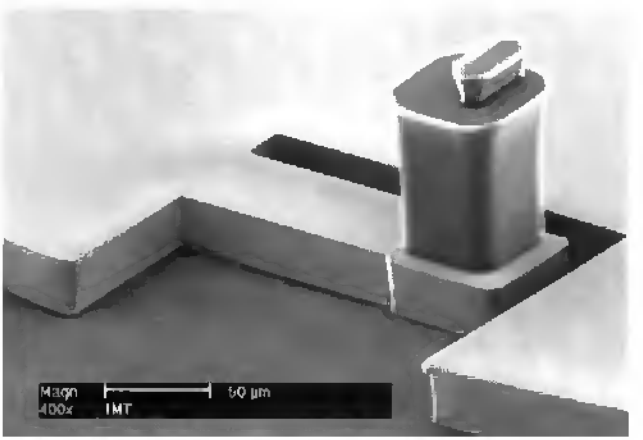

Fig. 3.23: Close-up view of a SU-8 leg of the rotor

The major disadvantage of the SU-8 is its lack of hardness. After a few rotations of the rotor, abrasion is observed on the contact point of the legs (Fig. 3.24).

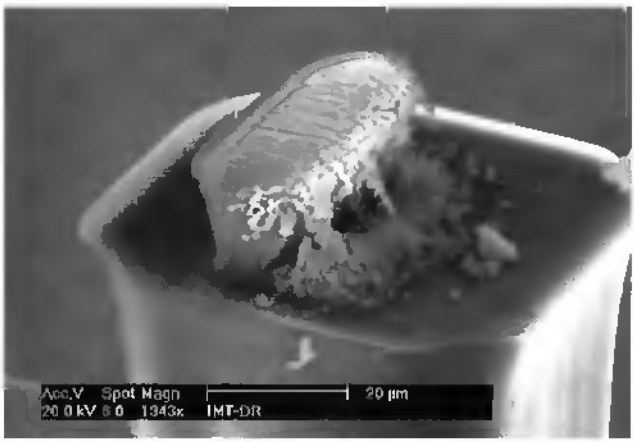

Fig. 3.24: Abrasion of an SU-8 leg after rotation.

This abrasion problem can be reduced by improving the SU-8 crosslinking during the hardbake, thereby creating a harder material.

3.8. The nickel legs

The SU-8 legs abrasion problem motivated the choice of an alternative fabrication method using nickel electroplating. This technology is more difficult and less reproducible than the SU-8 process, but produces a harder material.
This second method for fabricating the vertical legs in nickel used the positive thick resist process pushed to its technological limits. The illumination of thick positive resist layers is limited by light absorption in the material, and so that maximum thicknesses are situated around 120 µm. With such a thickness, the mould sidewalls are not very well defined and the nickel electrodeposition solution has difficulties penetrating into the mould.

A thick positive photoresist layer (Fig. 3.26) (AZ-4562 / 110µm) was directly spun on the electrodeposited nickel wheel (Fig. 3.25) using the rotating cover spinner.

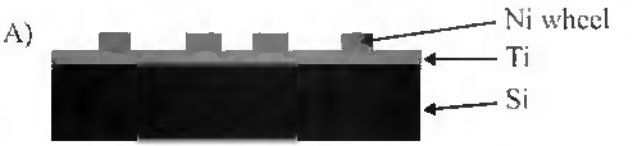

Fig. 3.25: Electrodeposited nickel wheel.

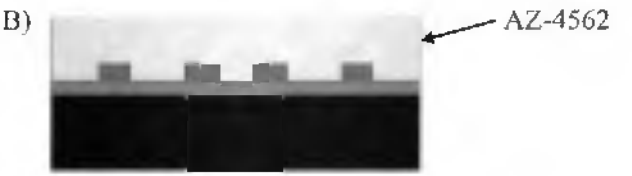

Fig. 3.26: Positive resist layer directly spun on the electrodeposited nickel wheel.

Prebake was realized with a ramped hotplate. The illumination was realized with the AL6-2 mask aligner in vacuum contact mode (Fig. 3.27). This improved structures definition by reducing diffraction effects.

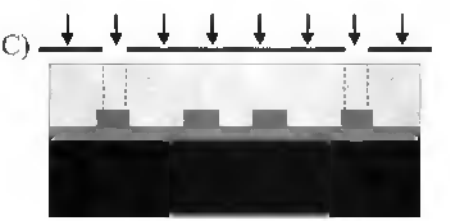

Fig. 3.27: Exposition of the resist layer.

During development with AZ-400K [1:3] (1 AZ-400K part for 3 parts DI water), the wafer had to be energetically agitated in the bath, enhancing the developer

penetration into the small mold structures (Fig. 3.28). The developing bath needed to be changed several times to avoid saturation.

Fig. 3.28: Development of the resist layer.

To avoid distortion of photoresist patterns, no postbake was done [6]. The resist mould was then treated in HCl, to clean the seed layer surface. To improve Nickel Sulfamate solution penetration into the small mould structures, the resist mould was treated with a wetting agent (Lea Ronal Wetting Agent). The nickel electrodeposition was then performed (Fig. 3.29), followed by the stripping of the resist mould (Fig. 3.30).

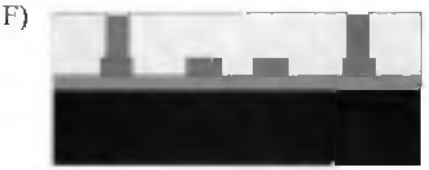

Fig. 3.29: Electroplating of the nickel in the resist mould.

Fig. 3.30: Stripping of the resist mould.

In the final step the fabricated structures were released by a sacrificial etch of the Ti in a HF solution (Fig. 3.31).

Fig. 3.31: Structures released by sacrificial etch of the Ti layer in HF.

Fig. 3.32 shows a nickel leg on the nickel wheel. The poor quality of the mould explains the different imperfections of the leg. The fin on the vertical side of the leg is due to a crack in the mould, and the angle of the sidewall is due to light absorption near the mould bottom during resist illumination.

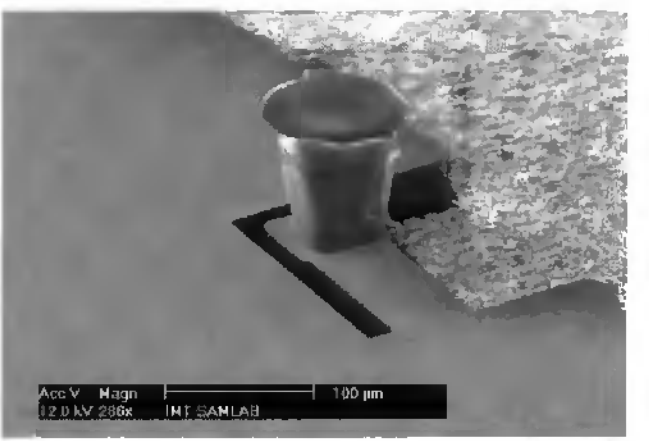

Fig. 3.32: Closed view of a nickel leg of the rotor.

This technology produces very hard legs, but with a very poor reproducibility when compared to the SU-8 process.

3.9. Characterization

3.9.1. Principle

Two motor characteristics are measured, namely the steady state speed and the dynamic torque. Several rotor types were characterized, both micromachined and laser cut CuBe (with inclined legs) rotors. The stator used for these measurements was a CuBe membrane glued on bulk PZT disk with an axle at its center (Chapter 2). This stator type was more resistant to mechanical shocks and more suitable for several rotor exchanges than the silicon stator (Chapter 2).
Measurements were performed with an optical setup (Fig. 3.33), which consisted of the PZT stator and a rotor loaded with an optical shutter and an optional mass. A laser spot was directed under the shutter by an optical fiber and collected by a photodiode.

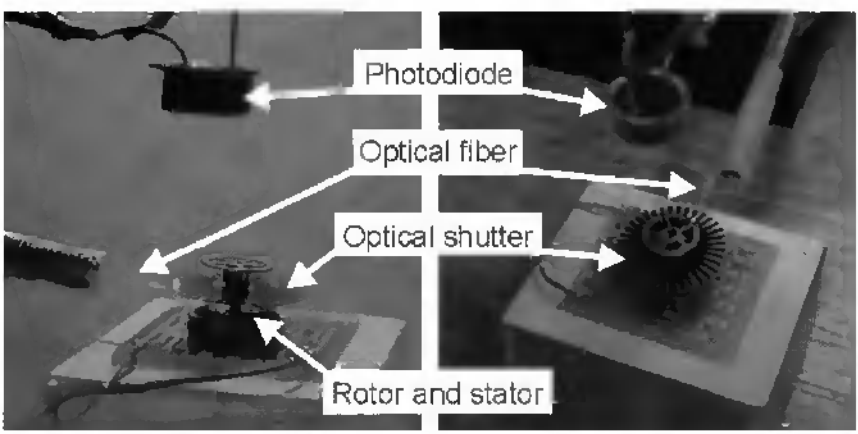

Fig. 3.33: Photographs of the setup used for rotor characterization (torque and speed).

A complete diagram of the experimental setup is shown in Fig. 3.34. The photodiode signal was amplified and digitized with a data acquisition card, which also controlled the motor operation at the same time. All these acquisition

steps were controlled with Labview, followed by the data processing with Matlab.

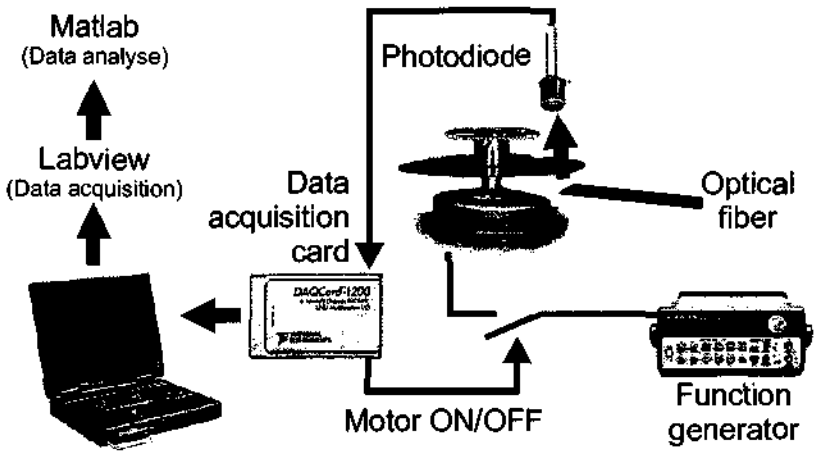

Fig. 3.34: Description of the data acquisition and processing steps.

Different motor operation sequences were performed, as dictated by the type of measurement (speed or dynamic torque) [10].

The revolution speed, , was measured by measuring the rotation angle, φ, as a function of time (= dφ/dt) for different preloading forces and rotor types. The data acquisition was done by switching on the motor, letting it accelerate, and then turning it off. These measurements were performed four times to increase the number of data points and obtain an average maximum acceleration.

The speed was calculated only after the rotor had reached a stable rotation speed (a few seconds).

The torque, T, which is proportional to the angular acceleration, can be calculated assuming a known inertial load J (calculated from the geometry and mass density of the load).

$$T = J\frac{d\Omega}{dt} = J\frac{d^2\varphi}{dt^2}$$

The acceleration of the rotor is obtained by the numerical derivation of the rotor speed. The acceleration is maximum during the transient period of operation (Fig. 3.35).

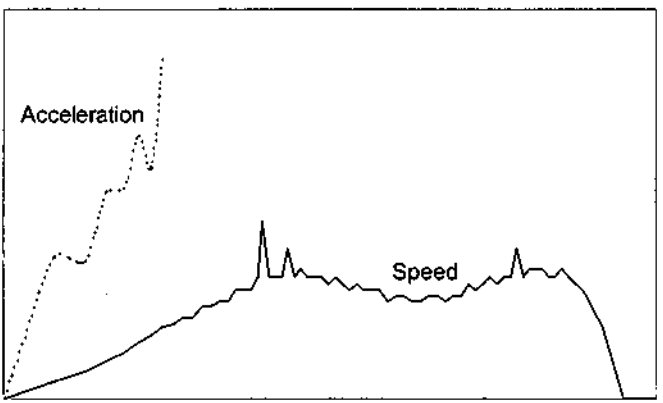

Fig. 3.35: Typical measured speed and calculated acceleration of a SU-8 type rotor.

3.9.2. Comparison of different rotor types

The steady state speed and dynamic torque were measured for three different types of rotors with different loading masses (preloading force).

3.9.2.1 CuBe rotor

Table 6: Speed and torque measurements for the CuBe rotor

Load [mg]	Speed [rad/s]	Torque max. [µNm]
3492	19.6	2.0
2001	27.2	1.1
1491	38.4	0.6

3.9.2.2 *Electrodeposited nickel rotor with SU-8 legs and* 200 µm elastic *beam*

Table 7: Speed and torque measurements for the SU-8 rotor with 200 µm elastic beam.

Load [mg]	Speed [rad/s]	Torque max. [µNm]
3492	25.2	2.7
2001	28.5	1.3
1491	35.7	0.9

3.9.2.3 *Electrodeposited nickel rotor with SU-8 legs and* 100 µm elastic *beam*

The measurement with the 3492 mg load exhibited erratic speed, due to weak conversion of the 100 µm beam. This made the torque measurement impossible.

Table 8: Speed and torque measurements for the SU-8 rotor with 100 µm elastic beam.

Load [mg]	Speed [rad/s]	Torque max. [µNm]
3492	~11	-
2001	17.4	0.8
1491	21.2	0.4

3.9.2.4 *Electrodeposited nickel rotor with nickel legs and 200 µm elastic beam*

The characterization of this type of rotor was difficult, due to the poor reproducibility of nickel leg thickness. This explains the mediocre results obtained in these measurements.

Table 9: Speed and torque measurements for the Ni rotor

Load [mg]	Speed [rad/s]	Torque max. [µNm]
2001	14.8	0.8

3.9.2.5 Summary

Fig. 3.36 shows a comparative chart of different rotors (CuBe, SU-8 and Ni legs) with different loading masses (3492 mg, 2001 mg and 1491 mg).

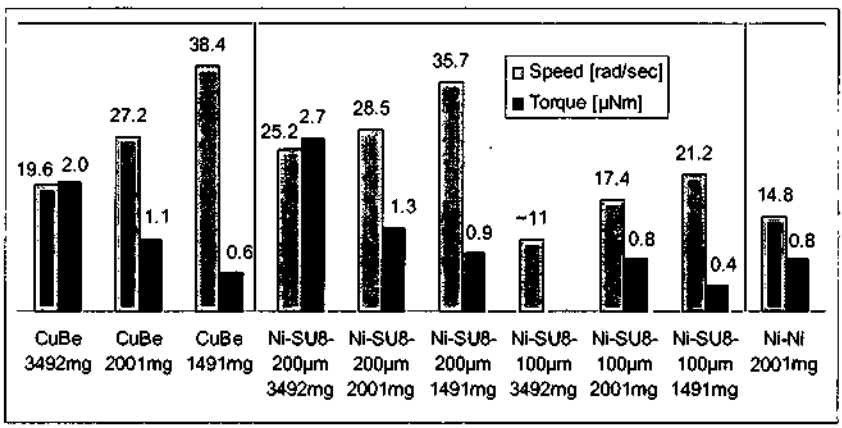

Fig. 3.36: Comparison of the different types of rotors with different loading masses.

The measurements presented in Fig. 3.36 show that the 200 µm SU-8 rotor produced a higher torque and speed than the CuBe one. This can be explained by the fact that the SU-8 design, with 3 or 6 legs, was less sensitive to a non uniform mode of vibration with a small number of legs, increasing the number of legs in contact with the stator. The thickness of the SU-8 legs was also much more reproducible than the CuBe case. The friction coefficient between the SU-8 and the CuBe stator being higher than between CuBe and CuBe could also explain the higher conversion ratio of the SU-8 leg.

These results shows that the dimensioning of the Ni rotor according to the CuBe design did not yield the most efficient design (L2=140 µm). The length of the elastic beam needs to be longer (L2=200 µm) to improve the conversion ratio. This can be explained by the fact that a more elastic beam disturbs the stator vibration less.

3.10. Conclusion

The development of a new rotor fabricated with microtechnologies resulted in a more efficient behavior and better dimensional reproducibility. The understanding and modelization of EFM function is very difficult, because many parameters are interrelated and therefore influence each other. A design based on simulation or analytical development of the different parts of the motor is then rendered unreliable. The most efficient way to design such complicated systems is by an empiric method.

The development of this new rotor design also stimulated the development of new technologies based on high-aspect ratio structuring of photopolymer and nickel electroplating.

The main advantages over past fabrication methods are better design flexibility, simplicity of the fabrication process, and the capability to combine metallic materials (Ni) with polymeric materials (SU-8).

This process opens the way to low cost fabrication of complex metallic and plastic structures for use in MEMS applications.

3.11. References

1. C. Beuret, G.-A. Racine, J. Gobet, R. Luthier and N. F. de Rooij, "Microfabrication of 3D multidirectional inclined structures by UV lithography and electroplating", MEMS '94, pp. 81-85.
2. L. Dellmann, S. Roth, C. Beuret, G.-A. Racine, H. Lorenz, M. Depont, P. Renaud, P. Vettiger and N. F. de Rooij, "Fabrication process of high aspect ratio elastic and SU-8 structures for piezoelectric motor applications", Sensors and Actuators, A Physical, vol. 70, 1998, pp. 42-47.
3. G. Engelmann, O. Ehrmann, J. Simon and H. Reichl., Development of a fine pitch bumping process, Micro System Technologies 90, Berlin, Germany, 10-13 September, 1990, pp. 435-440.
4. S. Roth & L. Dellmann, G.-A. Racine and N.F. de Rooij, "High aspect ratio UV photolithography for electroplated structures", Journal Micromechanical Microengineering, vol. 9, 1999, pp. 105-108.
5. M. Moreau, Semiconductor lithography principles, practices and materials, Plenum Press, New-York, 1988, pp. 459-467 and 500-506.
6. H. Miyajima, S. Furukawa and M. Mehregany, High aspect ratio photolithography with precise dimensional control, The Electrochemical Society Proceedings Volume 94-32, 1994, pp. 63-74.
7. K. Y. Lee, N. LaBianca, S.A. Rishton, S. Zolgharnain, J.D. Gelorme, J. Shaw and T.H.P Chang, Micromachining Applications of a high resolution ultrathick photoresist, J. Vac. Sci. Technol. B 13, 1995, pp. 3012-3016.
8. H. Lorenz, M. Despont, N. Fahrni, N. LaBianca, P. Renaud and P. Vettiger, EPON SU-8 : A low-cost negative resist for MEMS, MME '96, Barcelona, Spain, 21-22 October, 1996, pp. 32-35.
9. M. Despont, H. Lorenz, N. Fahrni, J. Brugger, P. Renaud, P. Vettiger, High aspect ratio, ultrathick, negative-tone near-UV photoresist for MEMS applications, MEMS '97, Nagoya, Japan, 26-30 January, 1997, pp. 518-522.
10. G.-A. Racine, R. Luthier and N.F. de Rooij, "Hybrid Ultrasonic Micromachined Motors", Proc. IEEE Micro Electro Mechanical Systems, Fort Lauderdale, USA, pp. 128-132, 1993.

4. Thick positive resist technology

4.1. Introduction

Photolithography was first developed for the quasi two-dimensional processes of microelectronics to transfer copies of a master pattern onto the surface of a solid material, such as the silicon wafer. With the emergence of micromechanics, more interest was generated for three-dimensional processes. In the early 1950s, Robbins and Schwartz [1] developed the bulk isotropic etching of silicon with mixtures of HF and HNO_3. In the mid-1960s, the Bell Telephone Laboratories started work on anisotropic Si etching, initially in mixtures of KOH, water, and alcohol, and later in aqueous KOH solutions. These etching technologies opened the way to the 3-D micromachining of silicon. Bulk micromachining, which is used to etch into both crystalline and non-crystalline materials, is limited with respect to achievable structure geometries. This motivated the development of surface micromachining features in the early 1960s [2]. In this technique, structures are built up, layer by layer, on the surface of a substrate. Dry etching defines the features in a thin surface layers and wet etching releases them from the bulk material underneath by undercutting. Surface micromachining as we know it today was first demonstrated by Howe and Muller in the early 1980s, with polysilicon used as structural material [3].

Bulk and surface micromachining technologies only allow the realization of deep grooves in the bulk and thin structures (a few microns) on the surface of planar substrates. In 1975, Romankiw and coworkers at IBM combined

electrodeposition and X-ray lithography [4]. They made high aspect ratio metal structures by plating gold in up to 20 μm thick X-ray-defined resist patterns. In 1982, Ehrfeld presented the LIGA technique [5], which consists of a thick layer of resist (from microns to millimeters of poly(methylmethacrylate) (PMMA)) structured by high energy collimated X-ray radiation exposure and subsequently developed to obtain a three-dimensional resist mold. The resist mold is filled by electrodeposition with a metal and the 3-D standing metal structure is released by removing the resist. Typical values for LIGA features are heights of 20 to 500 μm, minimum dimensions of 1 to 2 μm and surface roughness of 0.03 to 0.05 μm [6]. The generation of X-ray radiation is complicated and expensive, requiring the use of a synchrotron source. The masks used in LIGA differ substantially from those for the standard IC industry. The main difference lies in the absorber thickness. Very thick absorbers (>10 μm of Au vs. 0.1 μm Cr) and highly transparent mask substrates must be used in order to achieve a high contrast (>200), because of the low resist sensitivity, the resist layer depth, and the high exposure dose (hundred times higher than in the IC case). In spite of the advantages of very thick layers (up to mm) and very good surface roughness (less than 0.05 μm), the LIGA technology is very heavy and expensive. The construction costs of a typical synchrotron totals over 30 million Euro [6], restricting dramatically access to this technology. Since the advent of LIGA, an effort has been made to develop low-cost, commonly available processes that approximate LIGA results. This has motivated the development of different photolithography techniques for high aspect ratio structures. M. G. Allen [7] fabricated plating molds using photosensitive polyimide in conjunction with UV exposure. Several groups fabricated high aspect ratio molds for metal electroplating with photolithography [8,9,10], using commercially available highly viscous positive photoresist (Clariant AZ-4000 family) and near-UV light source. In the mid-1990's, IBM developed SU-8, a negative epoxy-based resist with a very low absorption coefficient [11]. High aspect ratios (>10) and straight

sidewalls in thick layers (>500 μm) are possible by applying standard lithography. The most problematic aspect of this resist is the stripping and the residual stress in the layer. This type of new high aspect ratio resist process has encouraged further developments of inexpensive LIGA-like technologies in the micromachining community.

The need for thick metallic structures for the micromotor application motivated the development of thick positive resist processes in our laboratory. Thick positive photoresists have many advantages. Their patterning is performed with standard photolithography equipment, they are easily strippable, and structures up to 100 μm can be realized. This chapter describes single and double layer processes to make thick resist molds of Clariant AZ-4562 (38 μm and 85 μm) with good reproducibility. Different problems related to thick photoresist patterning, such as edge beading and cracking of the resist, are discussed, and solutions proposed. Side walls are characterized after nickel electrodeposition. Results, process limitations and applications are presented.

4.2. The Clariant AZ-4562 positive resist

The Clariant AZ-4562 positive photoresist is a two-components formulation made of a polymer base, novolac resin (N), and a photosensitizer, diazonaphthoquinone (DQ) [12]. When a hydrophobic DQ is added to an alkali-soluble resin (N), the resin dissolution is inhibited (Fig. 4.1).

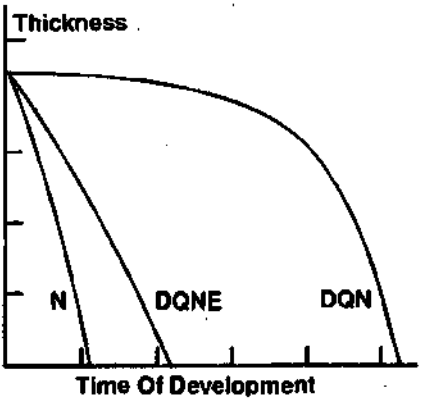

Fig. 4.1: Thickness versus time of development of novolak (N) film, diazonaphthoquinone mixed with novolak (DQN), and exposed diazonaphthoquinone in novolak (DQNE). From M. W. Moreau, "Semiconductors lithography principles, practices, and materials", Plenum Press New York, pp. 37, 1988.

During the photolysis (Fig. 4.2), the DQ generates a carbene (C) which rearranges to a ketene (K). The ketene reacts with absorbed moisture present in the resin to form an indene acid (A).

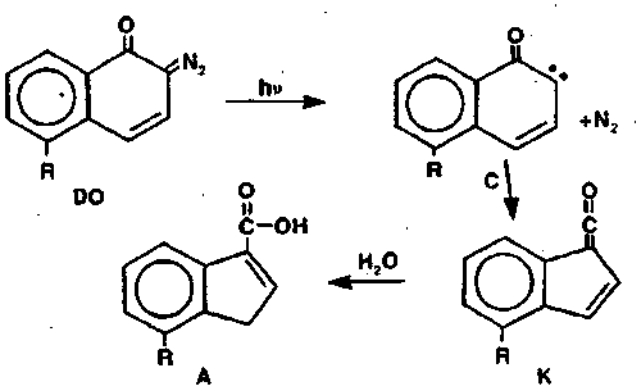

Fig. 4.2: Photolysis of the photosensitizer (DQ) into an indene acid (A), soluble in an alkali solution. From M. W. Moreau, "Semiconductors lithography principles, practices, and materials", Plenum Press New York, pp. 35, 1988.

The photochemical destruction of the inhibitor, and the release of uncomplexed resin induces upon development in an alkali solution, the dissolution of the exposed resist.

4.3. Coating of thick resist layers

4.3.1. Introduction

The thickness of a resist layer is determined by the spin coating speed: the slower the speed, the thicker the coated resist layer. As reported by Miyajima and Mehregany [13], a non-uniform coating is observed when the coating speed is too slow. This results in the contact between the mask and the wafer not being uniform enough to obtain high pattern resolution. The Gyrset RC8 (Karl-Süss, Germany) spin coater with a co-rotating cover (Fig. 4.3) allows the fabrication of thicker and more uniform resist layers in one single coating step. The solvent-saturated and co-rotating atmosphere created by the Gyrset system avoids drying of the resist and improves the homogeneity of the resist layer [14].
Two resist processes for different layer thicknesses (38 µm and 85 µm) were developed, taking into account in particular:

- process simplicity (with maximum two coating steps).
- minimization of the width of the peripheral region where edge-beading takes place, in order to maximize the useful wafer area.
- thickness uniformity.

Fig. 4.3: The RC8 spin-coater with co-rotating cover. The co-rotating cover allows the deposition of thicker and more uniform resist layers in one single coating step

4.3.2. Thick resist layer coating process sequences

4.3.2.1 The 38 µm thick resist layer process

The spinning sequence developed for the 38 µm thick layer process was used as a basis for the development of the 85 µm layer processes. It starts with a 30 second-long sequence at 110 rpm (Fig. 4.4). The accumulation of resist (edge beading) at the edge of the substrate prevents a good contact between the mask and the resist during the exposure step, decreasing the precision of the patterning (see § 4.5). The long spinning time [15] and the introduction of a short and huge acceleration (2000 rpm/s) in the middle and at the end of the spinning sequence reduced the width of the region in which the edge-beading took place.

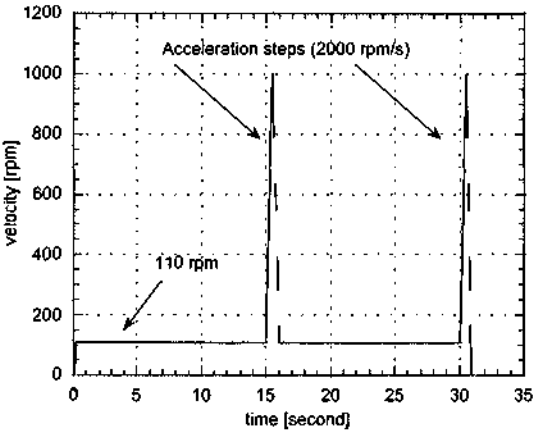

Fig. 4.4: Spinning sequence to achieve 38 µm thick resist layers, with a short and huge acceleration (2000 rpm/s) in the middle and at the end of the spinning sequence, to reduce the edge-beading effects.

4.3.2.2 The 85 µm thick resist layer process

To obtain the 85 µm thick resist layer, the 38 µm spinning sequence is performed twice with a short pre-bake in between. The final thickness is not the sum of two single coats of photoresist (i.e. 38+38 ≠ 85). This is because the adhesion of the second resist layer to the first is better than that of the first to the substrate, resulting in a greater thickness than expected [13].

4.4. Prebaking of the thick resist layers

4.4.1. Introduction

Prebake, also known as softbake or pre-expose bake, is the physical process of conversion of a liquid resist layer into a solid film. In the prebake step, the most of the solvent is evaporated without the degradation of the resist components.

Because of the relatively high boiling point of the solvent (>130°C), there always will remain a small amount of solvent left in the dried resist.

Since the prebake process can have an effect on subsequent processes such as exposure and development, the prebake is the most critical step of the thick resist process, and should be precise, uniform across the wafer, and reproducible. If the prebake temperature is too high, the photosensitive component may be partially degraded, and higher dose will be required for the exposure step. If it is too low, the solvent may interfere with the photolysis reaction, and different exposure-development parameters may be required. In fact, it influences the exposure energy and development time required, structural definition, the mold's side walls and aspect ratio [16].

To allow efficient evaporation of the solvent, the prebake is done on a ramped hotplate in a nitrogen environment. The heat input from the rear side of the wafer prevents crust formation at the top surface of the resist [17]. When the substrate is put in direct contact with the hotplate at bake temperature, the thick resist tends to flow to the center of the wafer. This phenomenon can be avoided by a programmed temperature ramp.

4.4.2. Thick resist layer prebake sequences

The 38 µm baking sequence is a temperature ramp from 40 to 90° C over 15 minutes, followed by a 60 minute plateau at 90° C. The 85 µm baking sequence involves two bakes. The first bake is performed after spinning the first resist layer, and consists of a 3 minute ramp from 40° to 80° C, followed by a 10 minute plateau at 80° C. The second bake is performed after spinning the second resist layer, and consists of a 15 minute ramp from 40° to 90° C, followed by a 150 minute plateau at 90° C. Table 4.1 summarizes the different prebaking parameters for the two layer thicknesses.

Table 4.1: Summary of the prebake parameters for the different layers thickness.

Layer Thickness	Starting Temperature	Final Temperature	Ramp Duration	Plateau Duration
38 µm	40° C	90° C	15 minutes	60 minutes
85 µm first	40° C	80° C	3 minutes	10 minutes
85 µm second	40° C	90° C	15 minutes	150 minutes

4.5. UV light photopatterning and nickel electroplating

4.5.1. Introduction

The positive AZ family of photoresists is sensitive to UV light. A mercury lamp is generally used as light source. For proper operation the light energy must be absorbed by the diazonaphthoquinone (DQ) photoactive compound which, when exposed, is converted into soluble indene carboxylic acid (E) (Fig. 4.5).

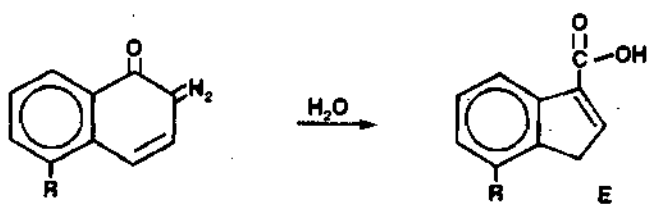

Fig. 4.5: Photolytic conversion of the photosensitizer (DG) into an indene acid (E), soluble in an alkali solution. From M. W. Moreau, "Semiconductors lithography principles, practices, and materials", Plenum Press New York, pp. 488, 1988.

One molecule of water per molecule of DQ is required to ensure this conversion [18]. If water is missing, the DQ will crosslink to an insoluble compound (Fig. 4.6), and exposed areas will not dissolve in developer.

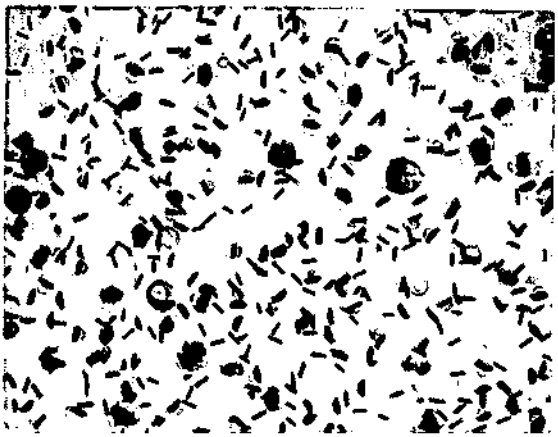

Fig. 4.6: DQ crosslinking to an insoluble compound (black dots), due to lack of water during exposure.

As the necessary water is not contained in the resist layer, a rehydration time is necessary to let the moisture being absorbed from the atmosphere (see section 4.5.2). For this reason, photolytic conversion of DQ to E will drastically fall off if humidity is below 30% RH. If the upper limit for humidity goes above 60% RH, the resist layer will absorb too much water, resulting in adhesion problems. For these reasons, a relative humidity of 45% is recommended. Exposed areas of resist are dissolved during development. Developers are aqueous alkaline solutions either based on sodium hydroxide (inorganic developers) or Tetra Methyl Ammonium Hydroxide TMAH (organic developers). The Clariant AZ-400K developer used in this process is based on NaOH bydroxide and buffered by borate. Temperature itself is not critical and room temperature is used (20 - 25 °C), however, it should be kept constant (±1 °C) for best process reproducibility.

The main difficulties of photopatterning thick resist layers with UV light are exposing the entire resist thickness, obtaining a maximum mold verticality, keeping a good pattern definition and avoiding resist peeling and cracking.

Different simple "tricks" can address these problems:

- A high exposure energy ensures illumination through the entire resist layer [19] and improves mold edge slope by reducing the required development time.
- Vacuum contact exposure mode improves pattern definition and mold edge slope by reducing diffraction effects over larger areas, compared to the hard-contact mode [13,20,21]. However, an edge-bead removal step is then necessary to establish a good vacuum contact between the mask and the resist layer.
- Resist peeling appears after long exposure times, due to the formation of nitrogen gas as the resist photoactive component reacts (Fig. 4.2). Increasing the resist prebaking reduces this phenomenon [22,23].
- A rehydration time of the resist is performed between the prebake and the resist exposure, to avoid layer cracking during edge-bead removal, exposure and development steps. The rehydration time strongly depends on the room temperature and humidity.

4.5.2. Rehydration time and edge-bead removal

Before the UV exposure, rehydration is performed, followed by edge-bead removal. The rehydration time strongly depends on ambient temperature and humidity. Table 4.2 presents the optimum rehydration time values determined empirically for a room temperature of 21°C ± 2°C and a room humidity of 45% ± 2 %. It also permits the reduction of the exposure energy and the development time. A decrease in the latter helps reduce the dissolution (by the developer) of unexposed resist regions.

Table 4.2: Optimum values of rehydration times determined empirically for each layer thickness.

Layer Thickness	Rehydration Time
38 µm	60 minutes
55 µm	140 minutes
85 µm	5 hours

The data points of Table 4.2 plotted x vs. $\sqrt{t}$ (Fig. 4.7) follow a straight line, as predicted by the Einstein-Smoluchowski equation [24], expressing the distance traveled by diffusing molecules (Eq. (1)).

$$x = \sqrt{2Dt} \tag{1}$$

Where: x: distance of the diffusion [cm].
D: diffusion coefficient [cm^2/s].
t: duration of the diffusion [min].

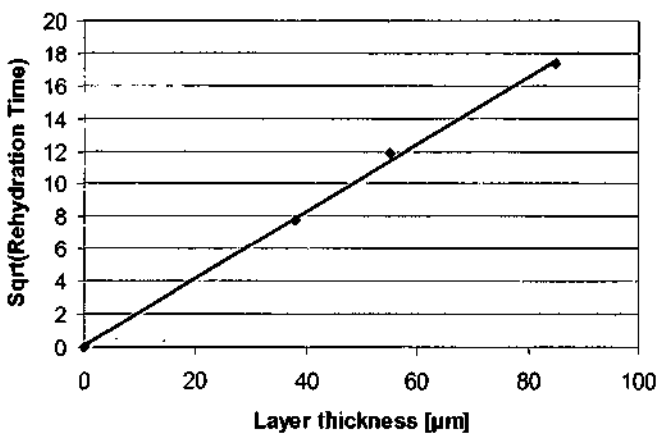

Fig. 4.7: Data points of Table 4.2 plotted x vs. $\sqrt{t}$.

The fact that this data exhibits this behavior shows that water diffuses into the resist layer during the rehydration time. At the end of this time, water is present throughout the membrane, having had time to diffuse a distance equivalent to the thickness of the resist layer. The observation that exposure energy and development times are reduced when optimized rehydration times are applied, is further evidence of this. Clearly, if the photolytic conversion of DQ to E is to be optimum, water must be present everywhere in the resist. Only then would it be possible to reduce both energy and development times. This model also allows the prediction of the rehydration times necessary for different resist thicknesses, hence speeding up process optimization.

The rehydration time is followed by the edge bead removal. It is performed by spinning the substrate at low velocity (500 rpm) and by spraying acetone with a syringe along the edge of the spinning wafer.

4.5.3. Exposure, development and post-bake of the thick resist layers

4.5.3.1 Process parameters

The exposure was performed with a mask aligner (Electronic Vision AL6-2, mercury lamp at 355 nm, 405 nm and 436 nm) in vacuum contact mode. Development was carried out with Clariant AZ 400K developer (one part developer diluted in four parts de-ionized water). The wafer was immersed and then energetically agitated in the bath to enhance developer penetration into the small mold patterns. Table 4.3 shows the exposure and development parameters for the 38 µm and the 85 µm thick resist layers on substrates with a metallic layer.

It was noticed that for thick resist layers which are spun onto silicon, silicon dioxide or silicon nitride layers, the exposure energy had to be reduced. The long exposure time generates local peeling of the resist. This phenomenon seems

to be related with adhesion problems [22], i.e. positive photo-resists have a better adbesion on metallic layers than on silicon "family" layers. HMDS primer treatment did not significantly improve thick resist layer adhesion. The last row of Table 4.3 gives the exposure and development parameters for coating on non-metallic layers. The concentration of the developer was changed (one part developer diluted in three parts de-ionized water) to compensate for the decrease in exposure energy.

Table 4.3: Exposure and development parameters for 38 μm and 85 μm thick resist layers on substrates with a metallic layer, and for 38 μm thick resist layers on non-metallic layers.

Layer thickness	**Exposure energy**	**Development time**	**Developer concentration**
38 μm	3500 mJ/cm^2	4 minutes	1:4
85 μm	4750 mJ/cm^2	10 minutes	1:4
38 μm (non-metallic layers)	650 mJ/cm^2	4 minutes	1:3

For electroplating applications, no post-bake was done after the development step, in order to avoid deformation of the resist mold [25]. If thick resist layers were used as protective layers for etching processes, a post-bake step of 15 min at 120°C on the hotplate was performed to stabilize the photoresist and avoid degassing during dry etching (Chapter 5).

4.5.3.2 Influence of the rehydration time on the exposure and development parameters

The introduction of a rehydration time allowed both the required exposure energy and the development times to be reduced. As the developer also dissolved unexposed regions of the resist, reduction of the development time

promoted improved mold edge-slopes. Table 4.4 gives some development time values for different rehydration times for the 38 µm thick resist layer.

Table 4.4: Influence of the rehydration time on the development time for the 38 µm process.

Rehydration time	Exposure energy	Development time
20 minutes	3500 mJ/cm^2	12 minutes
45 minutes	3500 mJ/cm^2	6 minutes
60 minutes	3500 mJ/cm^2	4 minutes

The Table 4.4 shows that when the quantity of water present in the resist layer is not sufficient, the photolytic conversion of DQ to E will drastically fall off, and by the way the development time is increased.

4.5.4. Nickel Electroplating

The wafer to be plated, masked with photoresist to define the regions onto which nickel is to be deposited, is maintained at a negative potential (the cathode) relative to the positive counterelectrode (the anode). The electroplating solution contains a reducible form of Ni ions. By biasing the surface to be plated with a negative potential, electrons are supplied to the surface of the exposed seed layer and Ni ions in the solution are reduced at the surface, resulting in nickel deposition.

The nickel electrodeposition reaction at the cathode, given in equation (2), competes with the hydrogen reaction at the same electrode, in equation (3).

$$Ni^{2+} + 2e^- \rightarrow Ni \qquad (2)$$

$$2H^+ + 2e^- \rightarrow H_2 \qquad (3)$$

The amount of hydrogen evolving and competing with Ni deposition depends on the pH, the temperature, and the current density. Since one of the most important causes of defects in the nickel microstructures is the appearance of hydrogen bubbles, these three parameters need precise control.

Impurities cause hydrogen bubbles to cling to the photoresist mold, resulting in pores in the deposited nickel layer. Therefore, the bath must be kept clean by circulating through a membrane filter. The main impurities are nickel hydroxide formed at increased pH-values in the cathode vicinity and organic decomposition products from the wetting agent. These problems can be avoided by monitoring and controlling pH and the adsorption of the organic decomposition products on activated carbon.

Before the nickel electroplating process, the substrate with the thick photo-patterned resist molds was dipped briefly in a 5% hydrochloric acid solution, to remove any oxide or organic impurities on the seed layer surface. A short dip into a wetting agent (Lea Ronal Wetting Agent) was also performed to improve the penetration of the plating bath into the very small structures of the mold. An illustration of the poor wetting can be seen in Fig. 4.8, where the nickel solution didn't penetrate completely into the mold. By dipping the mold into the wetting agent before plating, the formation of the nickel structures was improved (Fig. 4.9).

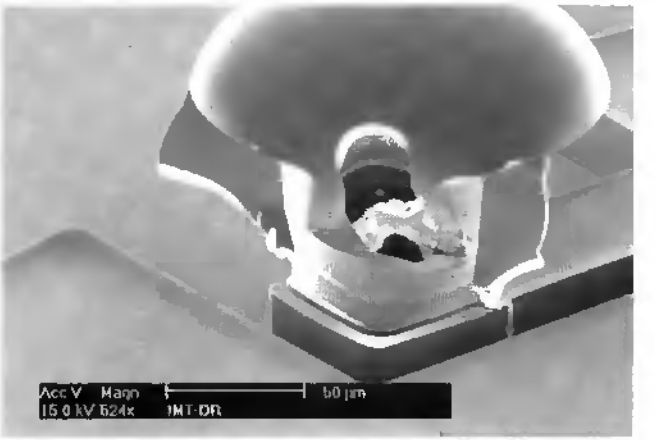

Fig. 4.8: The nickel solution didn't penetrate completely into the resist mold, resulting in a hole in the center of the nickel structure, due to the presence of air.

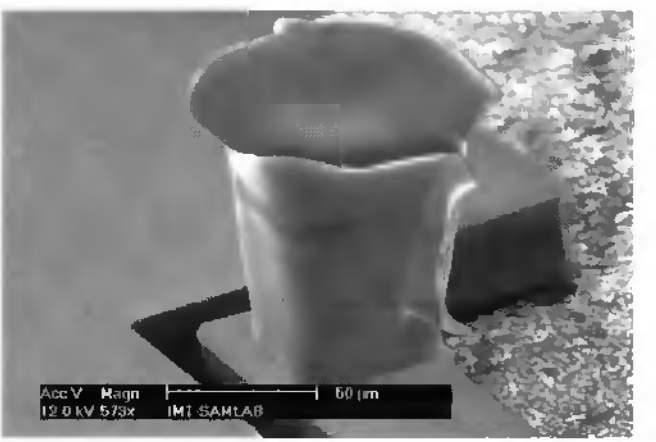

Fig. 4.9: By using wetting agent, the formation of the nickel structures was improved.

The nickel sulfamate bath composition, optimized for nickel electrodeposition, is a commercial product (Nickel Sulfamate type from Lea Ronal). The bath was operated at 55°C and at a pH value between 3.8 and 4.5. Metal deposition was carried out at current densities of 1 to 2 A / dm^2.

The metal electroplating had to be performed within a day following the photoresist mold fabrication. This is because mold deformation increased during the electrodeposition process after 24 hours. This phenomenon is due to hydration of the photoresist, which seems to weaken the photopatterned molds.

4.6. Results

4.6.1. Introduction

Results specifically related to particular applications are presented in Chapters 3 and 5. In this section, general results and process limitations of thick photoresist mold fabrication are presented. Many of these results presented were obtained after nickel electrodeposition and mold dissolution in acetone, as most of the applications for which the thick resist photopatterning processes were developed are directly related to nickel devices.

4.6.2. 38 μm thick resist molds and nickel structures

The 38 μm layer photopatterning process is the most optimized of the two which were developed. The reproducibility of the mold fabrication process was observed to be very good over the entire wafer (as long as the temperature and humidity of the room were stable around 21 ± 2° and 45% ± 2%).

4.6.2.1 38 μm thick resist molds

Fig. 4.10 shows a SEM picture of a structure made in 38 μm thick resist. The dimensions of the square on the mask were 20 μm x 20μm. The over-development of the resist reduced the dimension to 14 μm at the bottom and 12 μm at the top of the resist structure. The side walls are well defined over the whole height, and the resist top surface is uniform.

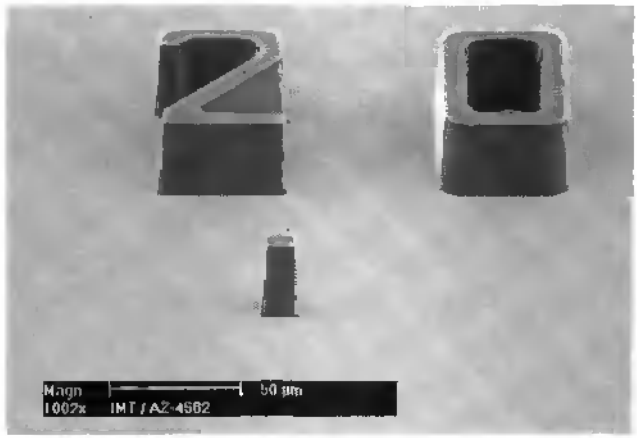

Fig. 4.10: SEM picture of a 13 µm (in the middle) wide square resist column.

Fig. 4.11 shows a 38 µm thick resist mold with a cylindrical hole of 10 µm diameter.

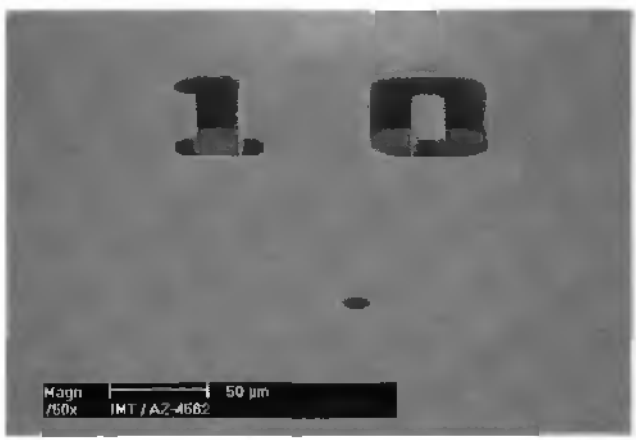

Fig. 4.11: SEM picture of hollow resist cylinder of 10 µm in diameter. The resist top surface is uniform.

Fig. 4.12 shows a test structure used to evaluate the exposure and the development parameters by optical measurements. It consists of two parallel

scales constituted of open lines on one side and filled lines on the other one. The reference position is defined by the central pair of open and filled lines, which have the same width on the mask. The over or under sizing of the structure after development is measured by counting the shift, from the reference lines, of the pair having the same width. Each shift corresponds to an enlargement or a reduction of 1 µm per line edge. In this case, a reduction of 4 to 5 µm is measured between the mask patterns and the top of the resist mold.

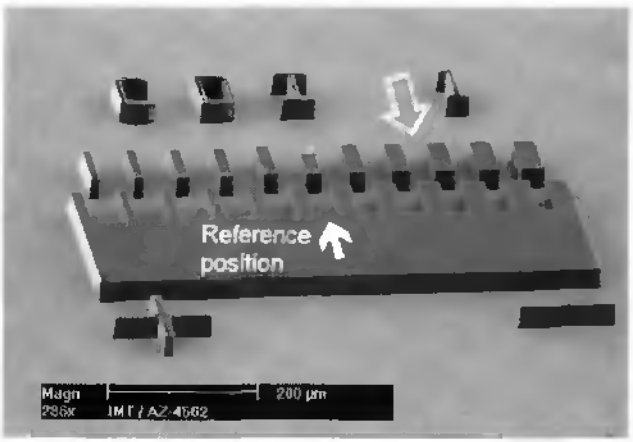

Fig. 4.12: SEM picture of a resist test structure used to define the enlargement or reduction between the resist and the mask patterns. A reduction of 4 to 5 µm is observed.

4.6.2.2 38 µm thick nickel structures

Fig. 4.13 shows a SEM of a 40 µm high and 14 µm diameter nickel cylinder. The "mushroom-like appearance is due to a nickel overgrowth in the mold. The definition of the mold wall is not so good at the top as at the bottom. This can be explained as a problem of light diffraction during the exposure step which generally affects the upper 20% of the resist thickness [20]. The edges of the structure are close to 90°.

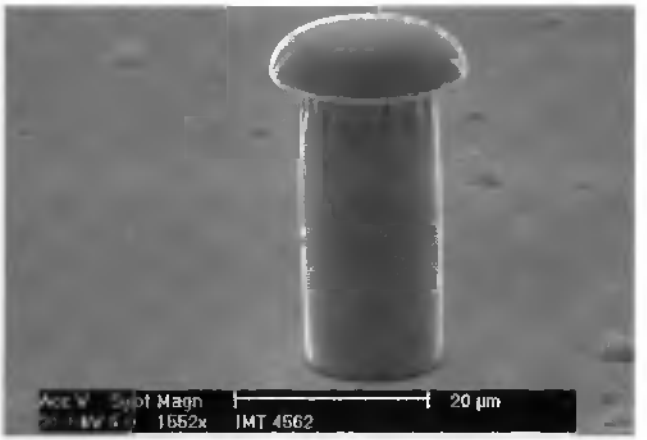

Fig. 4.13: SEM picture of a 40 µm thick and 14 µm in diameter nickel cylinder.

Fig. 4.14 shows a nickel comb test structure used to determine the smallest lateral distance between two opposite comb teeth (gap). On the mask, the tooth width is 4 µm and the gaps vary from 4 µm to 10 µm. Due to the mold enlargement, the realization of nickel combs with final gap sizes smaller than 2 µm becomes very difficult.

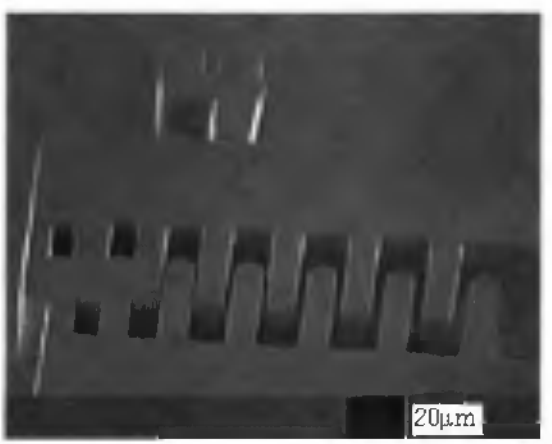

Fig. 4.14: SEM of a nickel comb like test structure with different gap sizes. The smallest measured gap of the nickel structure is 1.3 µm.

Fig. 4.15 shows a front view of the smallest nickel line realized with the 38 µm thick mold process. The line pattern is 1 mm long and 2 µm wide on the mask. The measured width is 7 µm. The "mushroom-like appearance is due to a nickel overgrowth in the mold.

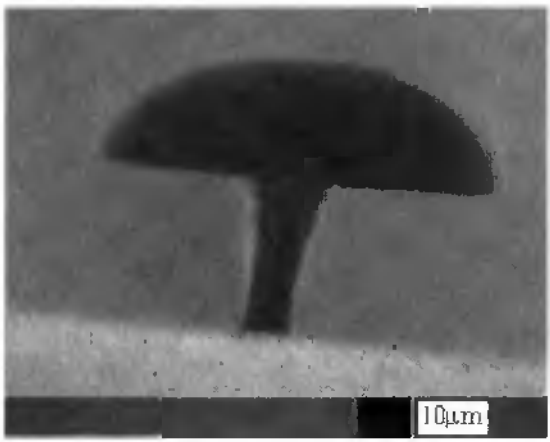

Fig. 4.15: SEM of nickel line with a 7 µm width (2 µm on the mask). This is the thinnest line realized with the 38 µm thick resist layer process.

4.6.3. 85 µm thick resist molds and nickel structures

The 85 µm thick resist layer photopatterning process was more delicate than the 38 µm one. The fabrication of molds with straight edge-slope has been rendered difficult, by the fact that the resist layer was very thick. Exposure and development therefore required long periods of time.

4.6.3.1 85 µm thick resist molds

Fig. 4.16 shows a SEM picture of a 85 µm resist structures. No division or horizontal line marks the interface between the two resist layers. The resist walls are well defined over the whole thickness.

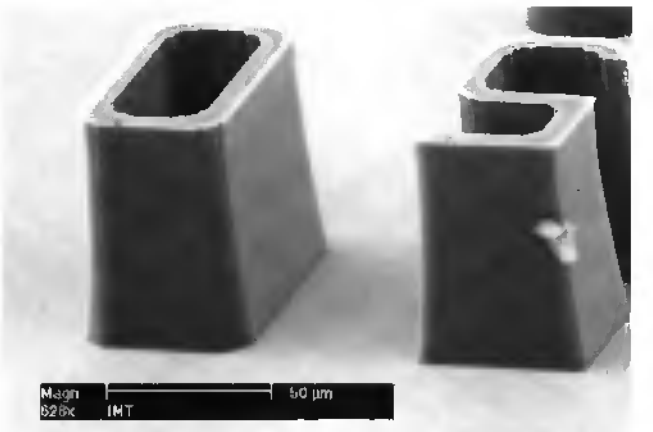

Fig. 4.16: SEM of an 85 µm thick resist mold. The mold is smooth over its entire height and no interface between layers is observed.

Fig. 4.17 shows a resist column structure with a square-shaped base of 20 µm on a side. Due to the relatively long development time and the isotropic nature of the developer, the top of the column is circular rather than square, as originally on the mask.

Fig. 4.18 shows a global view of a thick resist mold with hollow structures of different shapes (square, circle, hexagon and octagon). The hole dimensions are indicated by the numbers patterned near the structures. Holes with diameter down to 10 µm have been obtained.

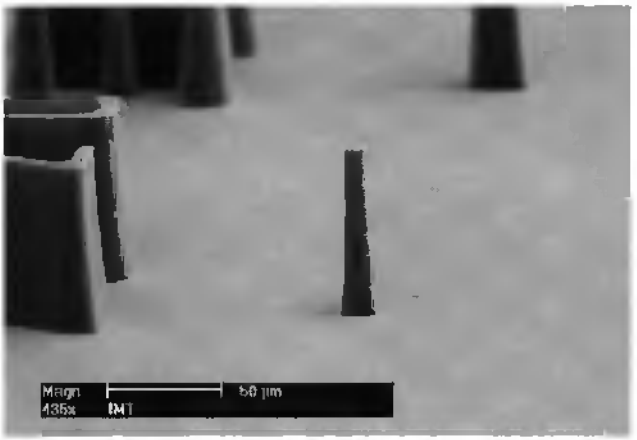

Fig. 4.17: SEM of a resist structure. The 20 µm wide square-base shape originally on the mask has become circular at the top.

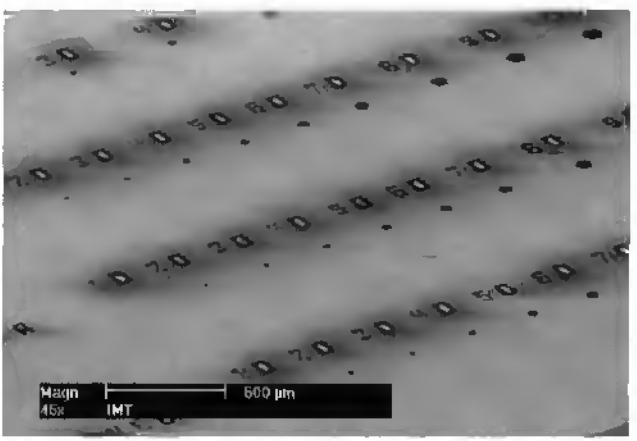

Fig. 4.18: SEM showing a global view of a thick resist mold for high aspect ratio Ni columns having different cross-sectioned shapes.

Fig. 4.19 shows a SEM of an 85 µm thick dimension control resist structure. The determination of the enlargement has the same working principle as explained above for Fig. 4.12. An enlargement of 3 µm per edge is measured.

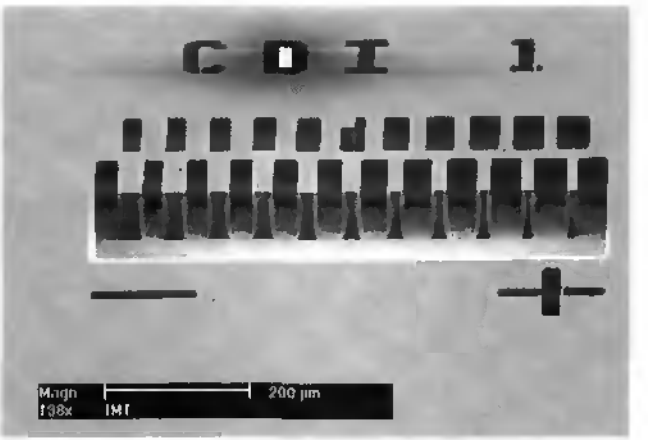

Fig. 4.19: SEM of an 85 µm thick dimension control resist structure. A 3 µm per edge enlargement is measured at the top of the mold.

Fig. 4.20 shows a SEM of a resist grid of 6 µm line width with a 18 µm pitch (on the mask).

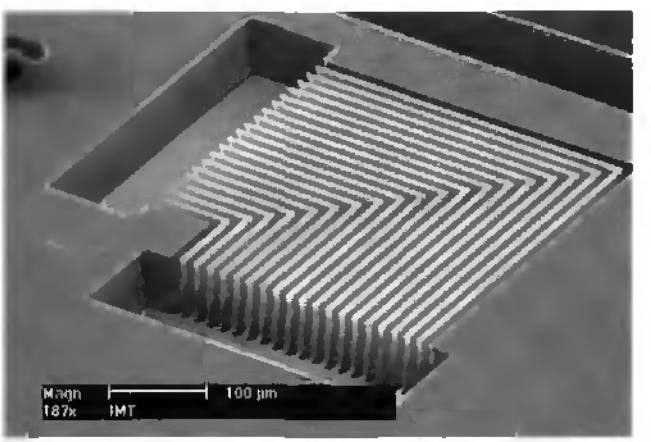

Fig. 4.20: SEM of an 85 µm thick line and space resist patterns. Lines width is 6 µm.

A close-up view of Fig. 4.20 is shown in Fig. 4.21. It shows the width limits of 85 µm high structures that can be obtained with this process. The underetching

at the top of the resist layer is due to the long development time and light diffraction effects. The surface of the resist layer is not over-etched so that the dimensions of the surface mold correspond to the mask dimensions. This is due to the formation of a thin crust at the resist surface during the prebake step, which decreases its solubility in the developer.

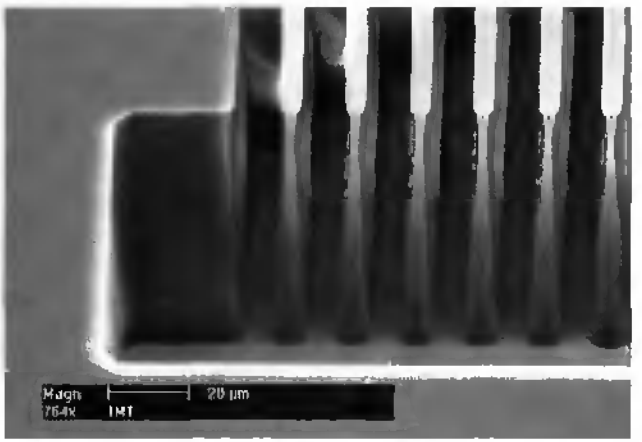

Fig. 4.21: Detail of the structure in Fig. 4.20. The "veils" visible between the lines on the left of the picture are SEM charging effects.

4.6.3.2 85 µm thick nickel structures

Fig. 4.22 shows a side view of an 85 µm thick T-shape nickel structure. No horizontal line at the resist layer interface is observed. Nickel overgrowing ("mushroom" like shape) delineates the height of the mold. It is observed that, as for the 38 µm thick layer process, the top of the mold has been deformed due to diffraction effects [20]. The slope angle of the sides is about 86°.

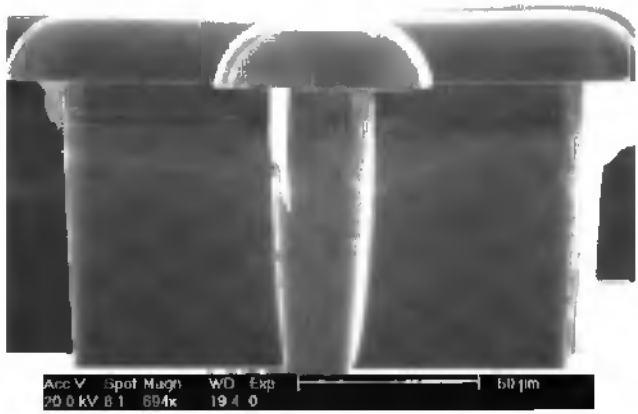

Fig. 4.22 SEM of 85 µm thick T-shape nickel structure.

Fig. 4.23 shows a nickel structure with a square base shape of 10 µm width on the mask, with a measured diameter of 16 µm at the bottom and 22 µm at the top of the structure. The wings located at the top of the nickel structure are due to a crack in the resist which formed during the electrodeposition, when the process was interrupted to measure amount of Ni deposited. The mold was taken out of the electrodeposition bath at 55 °C and the thermal shock caused cracks to appear in the resist layer. The line under the cracks indicates where the thickness measurement was done.

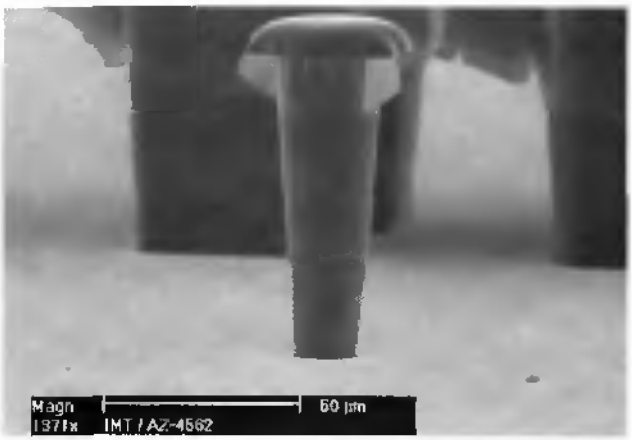

Fig. 4.23: SEM of square pattern on the mask with a measured diameter of 16 µm at the bottom and 22 µm at the top (10 µm on the mask).

Fig. 4.24 shows the smallest nickel line realized with the 85 µm thick mold process. The line pattern on the mask is 1 mm long and 4 µm wide. The measured structure width is 10 µm at half-height.

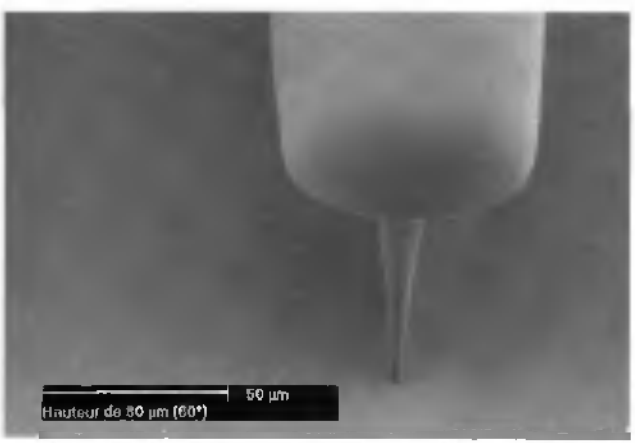

Fig. 4.24: SEM of a nickel line with a measured width of 10 µm at half-height (4 µm on the mask). This is the thinnest line realized with the 85 µm thick resist layer process.

Fig. 4.25 show a nickel grid of 11 µm wide lines and 13 µm wide spaces. The nickel electrodeposition has to be well regulated to avoid the overgrowth and to make the final structure usable.

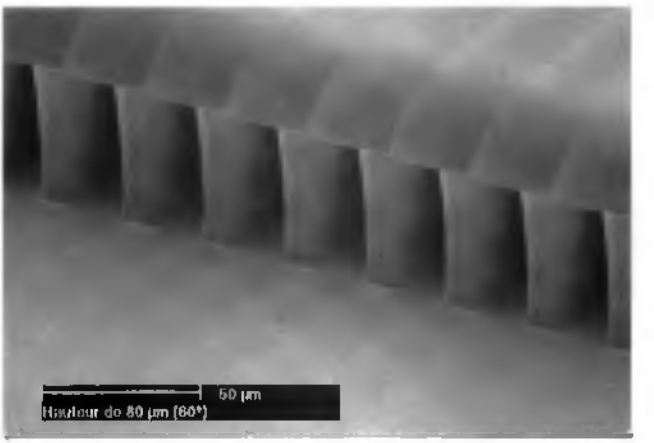

Fig. 4.25: SEM of a nickel grid of 11 µm wide lines and 13 µm wide spaces.

4.6.4. Discussion

The photopatterning of thick resist layer is obviously a capricious technology. Each step has non-negligible influence on the others. The results presented above show the wide range of applications of this technology. Edge-beading occurs during the coating process, and produces a layer 3 to 5 mm wide and 500-800 µm thick. The measured thicknesses are very uniform with 38 µm ± 5 % and 85 µm ± 5 %. The resist molds are easily dissolved by acetone despite the relatively long baking processes, and no residual resist was observed on any SEM of nickel structures.

The processes presented have some major limitations and requirements, which should be taken into account, and which are discussed below:

- The processes are reproducible as long as the temperature and the humidity of the room are stable (21°C ± 2°C and 45% ± 2 %).
- The rehydration times defined for different thicknesses should be respected. A change of the duration modifies the required exposure energy, can render the entire development of the mold difficult, and cause bubbles to be generated.
- The smallest line realized for the 38 µm process has a width of 2 µm on the mask and corresponds to a 7 µm wide nickel line. For the 85 µm process, the thinnest line on the mask is 4 µm, corresponding to a 10 µm nickel line.
- The measured enlargement between the mask and the resist patterns is 4-5 µm for the 38 µm process, and 3 µm for the 85 µm process.
- Because of enlargement of structures, compared to the mask, due to over development of the top of the mold, thin resist walls are more difficult to obtain than thin openings.
- For both processes, the surface area of electrodeposition has to be well known to avoid the overgrowth of nickel.

4.7. Conclusion

Thick resist technology has been demonstrated to be an attractive alternative to bulk or surface micro-machining. It is fully IC compatible. The processes have been developed with conventional photolithographic tools and with a commercially available photoresist. Spin coating sequences have been developed to minimize the edge-bead width and to obtain a layer thickness uniformity of 5%. A rehydration time has been introduced between the pre-bake

and the exposure steps to avoid resist cracks, usually appearing during the edge bead removal, the exposure and the development steps. It has been proven that it also reduces the required exposure energy and development time, and thus the etching by the developer of the unexposed resist. A single exposure step was performed for both the single and double layer processes. It was found that the exposure energy had to be drastically reduced and developer concentration increased for resist layers coated on non-metallic layers. The fabricated photoresist molds have been demonstrated to be fully compatible with nickel electroplating.

It has been noted that to avoid the overgrowth of nickel, the surface area of the electrodeposition has to be carefully calculated, which makes structures like combs or grids unusable, and can create undesirable short-circuits between closely spaced structures. No enlargement or shape structure distortion was observed between the resist molds and the final nickel structures.

The optimized processes have proven to be very reproducible and allow the fabrication of 38 μm and 85 μm thick resist molds with a yield close to 100%. Process limitations and requirements have been determined and guide lines for the design of MEMS processes have been established.

The development of thick resist processes was realized in collaboration with S. Roth, as a part of his thesis work.

4.8. References

1. H. R. Robbins and B. Schwartz, "Chemical etching of silicon-I. The system, HF, HNO_3 and H_2O", J. Electrochem. Soc., 106, pp. 505-508, 1959.
2. H. C. Nathanson, W. E. Newell, R. A. Wickstrom and J. R. Davis, "The resonant gate transistor", IEEE Trans. Electron. Devices, ED-14, pp. 117-133, 1967.
3. R. T. Howe and R. S. Muller, "Polycrystalline silicon micromechanical beams", Spring Meeting of the Electrochemical Society, Montreal, Canada, pp. 184-185, 1982.

4. E. Spiller, R. Feder, J. Topalian, E. Castellani, L. Romankiw, and M. Heritage, "X-ray lithography for bubble devices", Solid State Technol., April, pp. 66-68, 1976.

5. E. W. Becker, W. Ehrfeld, D. Munchmeyer, H. Betz, A. Heuberger, S. Pongratz, W. Glashauser, H. J. Michel and V. R. Siemens, "Production of separation nozzle systems for uranium enrichment by a combination of X-ray lithography and gavlanoplastics", Naturwissenschaften, 69, pp. 520-523, 1982.

6. M. Madou, "Fundamentals of microfabrication", CRC Press, pp. 275-323, 1997.

7. M. G. Allen, "Polyimide-based process for the fabrication of thick electroplated microstructures", Tech. Dig. 7th Int. Conf. Solid-State Sensors and Actuators, Yokohama, lapan, pp. 60-65, 1993.

8. E. W. Becker, W. Ehrfeld, P.Hagmann, A. Maner, D. Münchmeyer, Microelectronic Engineering. p. 435, 1986.

9. G. Engelmann, O. Ehrmann, J. Simon and H. Reichl, "Fabrication of high depth-to-width aspect ratio microstructures", Proceedings. IEEE Micro Electro Mechanical Systems, (MEMS'92), Travemünde, Germany, pp. 93-98, 1992.

10. B. Löchel, A. Maciossek, H.-J. Quenzer and B. Wagner, "UV depth lithography and galvanoforming for microfabrication", 186th Meet. Electrochem. Soc., Miami Beach, FL, pp. 100-111, 1994.

11. K. Y. Lee, N. LaBianca, S.A. Rishton, S. Zolghamain, J.D. Gelorme, J. Shaw and T.H.P Chang, "Micromachining Applications of a high resolution ultrathick photoresist",J. Vac. Sci. Technol. B 13, pp. 3012-3016, 1995.

12. M. W. Moreau, "Semiconductors lithography principles, practices, and materials", Plenum Press New York, pp. 34-38, 1988.

13. H. Miyajima and M. Mehregany, "High-aspect-ratio photolithography for MEMS applications", Journal of Microelectromechanical Systems, Vol. 4, No. 4, pp 220-229, 1995.

14. E. Cullmann, B. Loechel, A. Maciossek, M. Rothe, "Advanced resist processing for tick photoresist applications", Microelectronic Engineering 30, pp 551-554, 1996.

15. G. Engelmann, L. Dietrich, S. Gentzsch, R. Leutenbauer, R. Renger, H. Reichl, "Resist layer deposition and sacrificial layer technique in UV depth lithography and galvanoforming", Micro System Technologies' 96, Potsdam, pp 645-650, 1996.

16. M. W. Moreau, "Semiconductors lithography principles, practices, and materials", Plenum Press New York, pp. 329-333, 1988.

17. Hoechst Product Information Sheet, "Standard Photoresists AZ 4500-series", p.1, 1994.

18. M. W. Moreau, "Semiconductors lithography principles, practices, and materials", Plenum Press New York, pp. 488-506, 1988.

19. V. Conédédra, N. Fabre and M. Dilhan, " A simple optical system to optimise a high depth to width aspect ratio applied to a positive photoresist lithography process", J. Micromech: Microeng., 7, pp. 118-120, 1997.

20. E. Cullmann, B. Löchel and G. Engelmann, "Manufacture of 3D structures for micro systems with advances shadow casting lithography", Micro System Technologies' 94, pp 173-182, 1994.

21. E. Cullmann, "Belichtungs- und Justierungsuntersuchungen an extrem dicken Photolacken", proceeding of VDI / VDE-IT Erzeugung dreidimensionaler Mikrostructuren UV-Lithographie, München, 1997.

22. A. Kaway, H. Nagata, H. Morimoto and M. Takata, " Local peeling of photoresist film during ultraviolet exposure", Jpn. J. Appl. Phys., Vol. 33, Part 2, No. 1B, pp. L149-L151, 1994.

23. K. Suzuki, "Study on fine patterning processes with a thick resist", Sensors and Actuators A, 43, pp. 254-258, 1994.

24. I. N. Levine, "Physical Chemistry", second edition, McGraw-Hill Book company New-York, pp. 467-469, 1983.

25. H. Miyajima, S. Furukawa and M. Mehregany, "High aspect ratio photolithography with precise dimensional control", The Electrochemical Society Proceedings, Volume 94-32, pp 63-74, 1995.

5. Applications of the AZ-4562 technology

5.1 Introduction

The simplicity of use of the thick resist process allows its combination with any standard micromachining technique, opening the way to the fabrication of new 3-dimensional micro-electromechanical systems. A number of applications are listed below.

- Microfabrication of Si cantilever and integrated tip (AFM) with a probe for the optical near field (SNOM) [1]. The thick resist layer is used to pattern a pn-junction on the tip.
- Thick resist as protecting layer for protruding structures during wet and dry etching [2], this application is presented in details in the section 5.2
- Thick resist mask used for the deep reactive ion etching process [3]. For example, the fabrication of Pt-tip microelectrodes for extra-cellular monitoring of activity of brain slices [4].
- Thick resist for transferring micro-mechanical components (tips for scanning probe microscopy) from their original to a target wafer [5].
- Thick resist as mold for electrodeposition of nickel reed relay [6], rotor for the elastic force motor (Chapter 3), combined with SU-8 photostructuring [7], and the development of a clipping technology to assembly microfabricated structures [8], presented in details in section 5.3.

5.2 Protection of protruding structures during wet and dry etching processes

5.2.1 Introduction

A simple technique is proposed here, which can be used with a standard set-up for lithography (spinner and hot plate) to protect high aspect ratio protruding structures, in this case sharp atomic force microscope (AFM) tips, in wet and dry etching.

5.2.2 Tips fabrication and thick photoresist patterning

Tips were fabricated [9] using an oxidized silicon wafer. Caps were patterned using standard photolithography and buffered hydrofluoric (BHF) acid. The wafer surface was then etched in potassium hydroxide (KOH), with the underetching effect being used to form the tips. As silicon etching in KOH is strongly anisotropic, the tip is formed by the intersection of crystallographic planes, and can thus be very sharp. A 4000 Å thermal silicon dioxide layer is then grown on the wafers, to be subsequently used for the wet etching experiments.

A thick positive photoresist layer (AZ-4562 / 40μm) was spun for the lithography process with a rotating cover spinner (Karl Süss RC8 Spin Coater). The prebake was realized with a hotplate. To improve resist adhesion, a temperature ramp of 40°C to 90°C was used, after which the temperature was maintained for one hour at 90°C.

The photopatterning of the resist around the tip was realized with a mask aligner (Electronic Vision AL6-2, mercury lamp 355nm, 405nm and 436nm) in proximity mode, and developed with AZ-400K [1:3] (1 part AZ-400K for 3 parts de-ionized water). A post-bake step of 15 min at 120°C is performed to stabilize the resist layer, and to avoid degassing during dry etching experiments.

5.2.3 Results

The first experiment consisted in protecting an oxidized tip with a photoresist hemisphere during a BHF etching. Fig. 5.1 shows the photoresist hemisphere after the postbake, with a diameter at its base of about 115 µm and a height of about 50 µm. The mask was a 120 µm disc and the photoresist thickness before postbake was about 40 µm. The tip is completely covered and protected within the hemisphere.

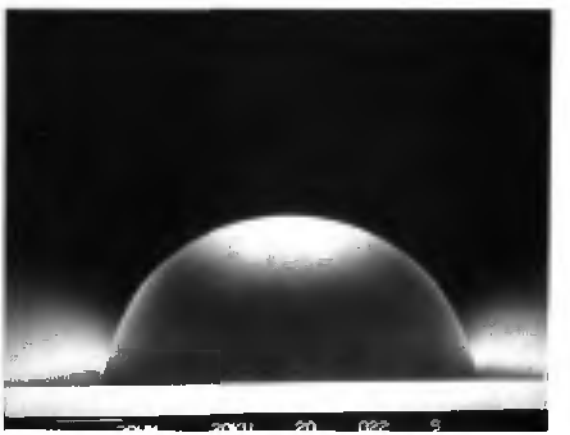

Fig. 5.1: Photoresist hemisphere after postbake. (Scale bar is 20 µm)

Fig. 5.2 shows an oxidized tip after oxide etching in BHF and photoresist removal. The insert in Fig. 5.2 shows a close-up view of the very top of the tip and demonstrates that it was perfectly protected during the wet etching.

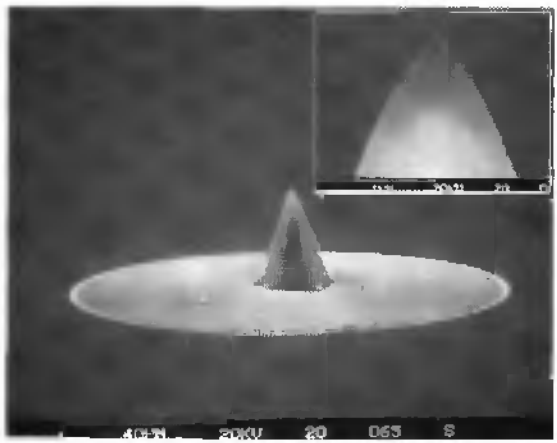

Fig. 5.2: Oxidized tip and oxide disc after BHF etching and photoresist removal. The insert shows a close up view of the top of the tip.

The second experiment consisted in defining the shape of a cantilever beam around the tip by deep reactive ion etching (DRIE). Fig. 5.3 shows a tip on a 300 µm thick cantilever beam. A close-up view (Fig. 5.4) of the very end of the tip in Fig. 5.3 shows that it was perfectly protected during the etching.

Fig. 5.3: Trenches about 300 µm deep, realized by dry etching.

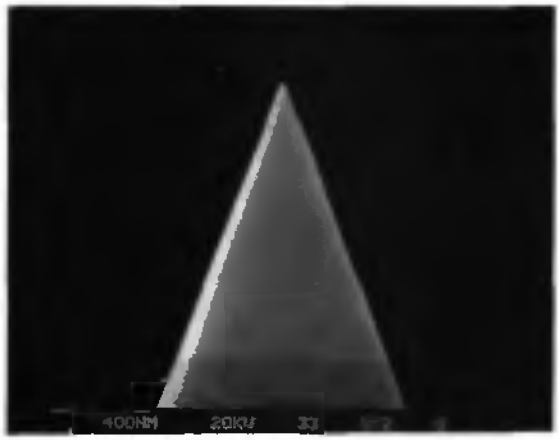

Fig. 5.4: Very top of the tip in Fig. 5.4 Estimated apex radius: less than 10 nm.

5.2.4 Conclusion

The technique presented here is convenient for the protection of protruding structures in wet and dry etching processes. As the covering photoresist layer is thick, deep dry etching can be performed to depths up to 300 µm without damaging the structures. Nevertheless, the thickness of the photoresist and its contraction during the postbake reduces drastically the lateral resolution of the lithography to about 25 µm. In spite of its low resolution, the technique which was presented above should be useful in many micromachining applications.

The development of the process for protection of protruding structures in wet and dry etching processes was realized in collaboration with P.-F. Indermühle and S. Roth, as a part of their thesis works.

5.3 Clip assembling technology

5.3.1 Clipping technique

The clipping technology was developed in order to realize assembly without any additional material, such as glue, or conventionally machined elements. The device to be clipped down was maintained on the axle with a clip (Fig. 5.5), designed to let pass the rotor during the mounting. The clipping procedure was realized by pressing the center of the device to be clipped down on the top of the axle clip with a pressing tool mounted on micro-manipulators. The buckling parts of the device to be clipped (Fig. 5.6) are elastically deformed when slipped under the axle clip.

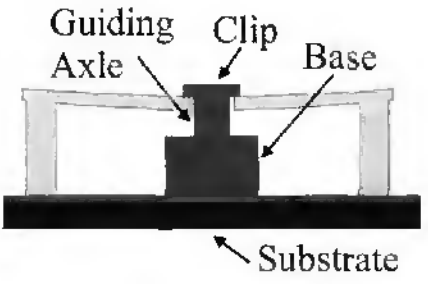

Fig. 5.5 : Schematic view of the clipping principle.

Fig. 5.6: Drawing of the buckling tongues around the hole of the clipped device.

The design of the buckling tongues was determined by using static finite element simulation (Fig. 5.7). To avoid plastic deformation of the tongues, the stress induced the tongues during the clipping operation should not exceed the elastic domain of the electroplated nickel (Fig. 5.8).

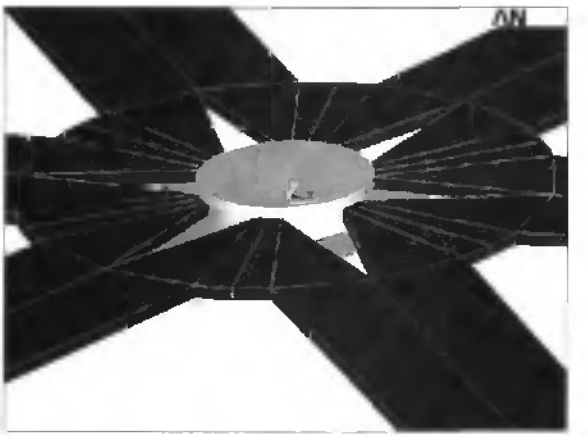

Fig. 5.7: Finite element simulation (ANSYS®) of a rotor clipped unto a micro-fabricated axle. The elasticity of the tongues in this rotor design is such that their plastic deformation during the clipping is avoided.

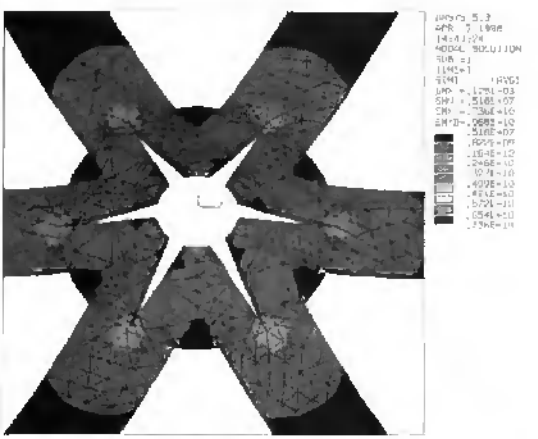

Fig. 5.8: Simulated stress induced by the clipping operation in the elastic tongues.

A special instrument was designed for the clipping technique (Fig. 5.9). It consisted of two parts. The first was a platform holding the axle chip, which could be controlled in the X-Y directions by two micro-metric screws. The second part was a vacuum syringe, whose position in the Z direction could be

controlled by a micro-metric screw. The device to be clipped was maintained on the syringe by vacuum and then pressed on the top of the axle clip in order to perform the clipping.

Fig. 5.9: The device to be clipped held by the vacuum syringe, ready to be clipped onto a microfabricated axle. The syringe is then lowered to realize assembly of the device.

5.3.2 Fabrication of the axle clip

The axle clip consists of a three level nickel structure (Fig. 5.5). The first one (the base), which is large, anchors the axle to the substrate. The second has the real guiding function and the third one is the clip itself (cover), which maintains the clipped device.

The new fabrication process is schematically presented in Fig. 5.10 to Fig. 5.17. Initially, a silicon wafer was prepared with a metallic seed layer (500 Å Cr/ 5000 Å Au). A 70 µm thick SU-8 layer (Fig. 5.10) was spun on, thermally cured on a temperature-ramped hot-plate, exposed with a standard UV light mask aligner and developed in PGMEA [10,11]. Next, the first nickel level was electrodeposited into the SU-8 mold with a commercial nickel sulfamate bath at 55°C (Fig. 5.11). A 40 µm thick AZ-4562 positive layer (Fig. 5.12) was spun on

and thermally cured on a ramped hot-plate [12,13]. The second level was exposed through the whole AZ-4562 layer (Fig. 5.13). The third level (Fig. 5.14) was exposed down into only the first few microns of the AZ-4562 layer, by adjusting the exposure dose. After development of the positive resist layer (Fig. 5.15), the nickel electrodeposition (Fig. 5.16) was performed, followed by dissolution of both molds (Fig. 5.17) in a commercial SU-8 remover.

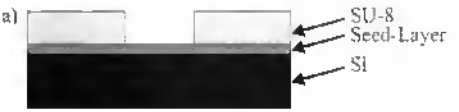

Fig. 5.10: Spinning of the SU-8 layer, thermal treatment, exposition and development.

Fig. 5.11: Nickel electrodeposition in the SU-8 mold.

Fig. 5.12: Spinning of the AZ-4562 positive layer and thermal treatment.

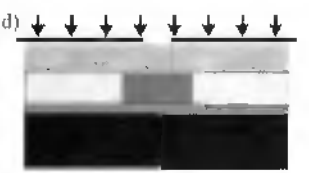

Fig. 5.13: First exposure of the positive layer to define the guiding level.

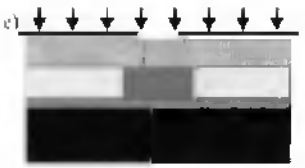

Fig. 5.14: Second exposure of the positive layer to define the clip level.

Fig. 5.15: Development of the positive layer.

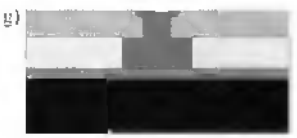

Fig. 5.16: Nickel electrodeposition in the positive resist mold.

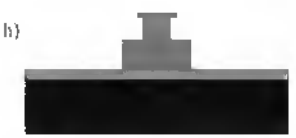

Fig. 5.17: Stripping of both resist layers.

5.3.3 Results

Fig. 5.18 presents a three-level nickel clipping axle on a Si chip.

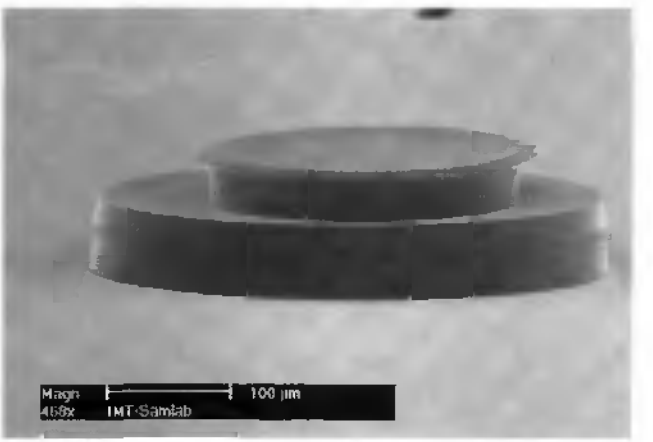

Fig. 5.18: Overview of the three-level nickel clipping axle on a Si chip. The base level is 60 µm high and 400 µm in diameter. The guiding level, without the clip, is 25 µm high and 200 µm in diameter.

Fig.5.19 shows the two top levels of an axle clip, the guiding level and the clip level. The double exposure of the AZ-4562 photoresist layer permits the realization of both top layers in the same mold. This avoids the technological complications that arise when using a mold for each level, such as curing and electrodeposition problems for the third level.

Fig.5.20 shows the micromachined nickel device to be clipped before being released from the wafer. The buckling parts composed of small tongues, schematically presented in Fig. 5.6 and in Fig. 5.7, can be seen in the center of the picture. The device was realized by nickel electrodeposition in photoresist molds on a separate substrate.

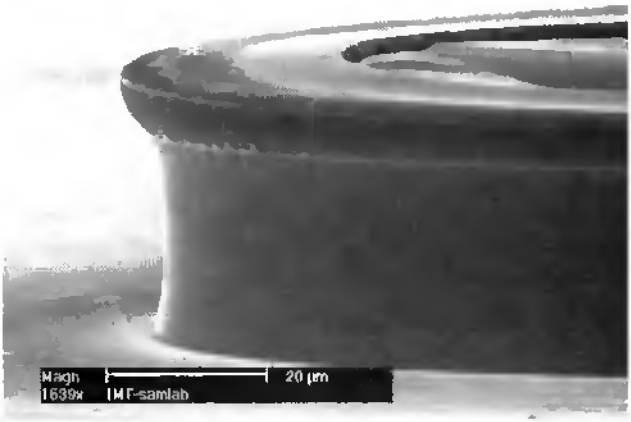

Fig.5.19: Detail of the top two levels of the microfabricated axle clip. Both nickel levels were realized in one electrodeposition step, in order to improve the thickness and side-wall control.

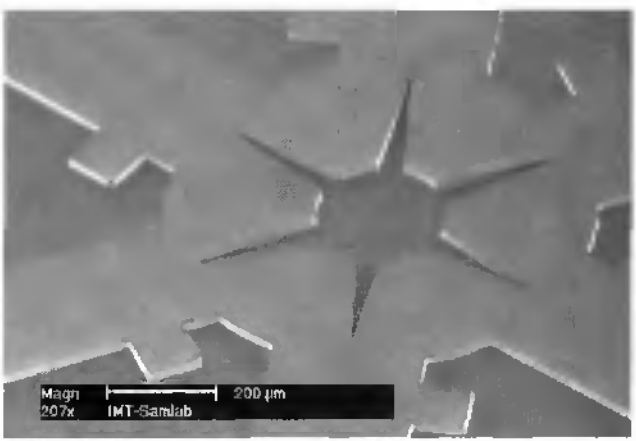

Fig.5.20: Detailed view of the buckling tongues before release from the substrate. The thickness is 15 µm.

Fig.5.21 shows details of the axle clip with a device clipped onto it. The clipping procedure was realized by pressing the center of the rotor down on top of the axle with a pressing tool mounted on micro-manipulators. The buckling parts of the rotor were elastically deformed when slipped under the axle clip.

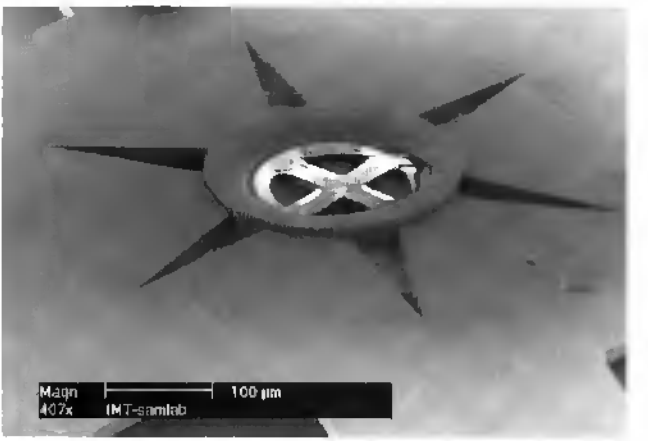

Fig.5.21: Detail of the device clipped onto the integrated axle clip. Traces or deposits left by the pressing tool, used during the clipping operation, can be seen around the axle. The white cross in the middle of the axle clip is a leftover SU-8 not dissolved, when the resist layers were removed.

5.3.4 Conclusions

The clipping of a device onto the multilevel axle clip demonstrates the feasibility of clipping parts with microfabrication technologies, without any additional material, such as glue, or conventionally machined elements. The combination of the two resists (SU-8 and AZ-4562) provided a good technological flexibility for multi-level electrodeposition. The advantage is the stability of the first SU-8 level with respect to the subsequent more critical levels. The use of a positive tone resist for the realization of the second and the third levels permitted very precise control of axle size and verticality of the

walls. This was achieved by performing a double exposure and single development of the same AZ-4562 layer.

The development of clipping technique was realized in collaboration with S. Gautsch, as a part of his diploma work.

5.4 Conclusions

Thick resist layers have been used to realize molds for nickel electrodeposition, the patterning of silicon for deep reactive ion etching, the protection of protruding structures during wet and dry etching, and the patterning of metal layers by lift-off into deep grooves. It is fully IC compatible and can be used to realize or transfer 3-D structures directly on IC substrates. The simplicity of use of this process allows its combination with any standard micromachining technology. All these applications demonstrate that the thick resist technology is a really inexpensive and attractive alternative to LIGA, bulk or surface micromachining.

5.5 References

1. G. Schürmann, W. Noell, U. Staufer, N. F. de Rooij, "Microfabrication of a combined AFM-SNOM sensor, Ultramicroscopy 82, pp. 33-38, 2000.
2. P.-F. Indermühle, S. Roth, L. Dellmann, and N. F. de Rooij, "Patterned thick photoresist layers for protection of protruding structures during wet and dry etching processes", J. Micromech. Microeng., 8, pp. 74-76,1998.
3. P.-A. Clerc, L. Dellmann, F. Grétillat, M.-A. Grétillat, P.-F. Indermühle, S. Jeanneret, Ph. Luginbuhl, C. Marxer, T.L. Pfeffer, G.-A. Racine, S. Roth, U. Staufer, C. Stebler, P. Thiébaud, N.F. de Rooij, "Advanced deep reactive ion etching: a versatile tool for micromechanical systems", Journal of Micromechanics and Microengineering, vol. 8, pp. 272-278, 1998.
4. P. Thiébaud, C. Beuret, M. Koudelka-Hep, M. Bove, S. Martinoia, M. Grattarola, H. Jahnsen, R. Rebaudo, M. Balestrino, J. Zimmer, Y. Dupont, "An array of Pt-tip

microelectrodes for extracellular monitoring of activity of brain slides", Biosensors & Bioelectronics, vol. 14, pp. 61-65, 1999.

5. T. Akiyama, U. Staufer, N.F. de Rooij, "Wafer- and piece-wise Si tip transfer technologies for applications in scanning probe microscopy", IEEE Journal of Microelectromechanical Systems, vol. 8, no. 1, pp. 65-70, 1999
6. S. Roth, C. Marxer, G. Feusier, N. F. de Rooij, "One mask nickel electroplated reed relay, Proc. MEMS'2000, Miyazaki, Japan, pp. 176-180, 2000.
7. L. Dellmann, S. Roth, C. Beuret, G.-A. Racine, H. Lorenz, M. Depont, P. Renaud, P. Vettiger and N. F. de Rooij, "Fabrication process of high aspect ratio elastic and SU-8 structures for piezoelectric motor applications", Sensors and Actuators, A Physical, vol. 70, 1998, pp. 42-47.
8. L. Dellmann, S. Gautsch, G.-A. Racine, N. F. de Rooij, "New integrated axle fabrication for piezoelectric motors based on a rotor clip assembling operation", Digest of Technical Papers 10th Internat. Conf. on Solid-State Sensors and Actuators, TRANSDUCERS '99, Sendai, J, pp. 1752-1755, 1999.
9. O.Wolter, Th.Bayer and J.Greschner, "Micromachined silicon sensors for scanning force microscopy", J. Vac. Sci. Technol., B 9, pp. 1353-1357, 1991
10. L. Dellmann, S. Roth, C. Beuret, G.-A. Racine, H. Lorenz, M. Depont, P. Renaud, P. Vettiger and N. F. de Rooij, "Fabrication process of high aspect ratio elastic and SU-8 structures for piezoelectric motor applications", Sensors and Actuators, A Physical, vol. 70, pp. 42-47, 1998
11. K. Y. Lee, N. LaBianca, S.A. Rishton, S. Zolgharnain, J.D. Gelorme, J. Shaw and T.H.P Chang, "Micromachining Applications of a high resolution ultrathick photoresist",J. Vac. Sci. Technol. B 13, pp. 3012-3016, 1995.
12. S. Roth, L. Dellmann, G.-A. Racine and N.F. de Rooij, "High aspect ratio UV photolithography for electroplated structures", Proc. Micromechanics Europe '98, Ulvik, N, pp.55-58, 1998.
13. H. Miyajima, S. Furukawa and M. Mehregany, "High aspect ratio photolithography with precise dimensional control", The Electrochemical Society Proceedings Volume 94-32, pp. 63-74, 1994.

6. Conclusions

The many advantages of the piezoelectric motors, such as high power density, low voltages, holding torque and low noise operation, have motivated in the beginning of the 90's, the development of the first hybrid generation of elastic force motors (EFM) using microfabrication technologies. Only the stator with a ZnO piezoelectric layer was microfabricated, while the rotor was realized with standard fabrication technologies. The goal of this thesis was to improve the first hybrid EFM, and to obtain a micromotor compatible with industrial production. To achieve this, several technological processes and designs have been developed or improved.

The new microfabricated stator with a ZnO piezoelectric layer allows the use of the first vibrationnal mode of the membrane, and has proved increased mechanical amplitude of the oscillation, in comparison to early stator design.

The free standing membrane, anchored in the middle, was fabricated using deep reactive ion etching technology and was actuated with an integrated ZnO piezoelectric layer. One of the most important problems encountered during the development of this process, was the reproducibility of the ZnO sputtering deposition. The poor quality of the piezoelectric layer limits the introduction of such products to the market, and needs to be drastically improved, to insure a reproducible mechanical behavior of the stator and a better fabrication yield.

The microfabricated stator exhibited good mechanical and electrical behavior. The motor was operated at a frequency of 20 kHz and with a typical excitation voltage of 4 V. The characterization of the motor was difficult, because of the fragility of the too thin stator membrane (20 μm), thereby no speed or torque

measurement of the complete microfabricated motor was possible. This problem shows the difficulty to manipulate microfabricated structures and should be taken into account when designing the next generation. The principle of the axle has to be reconsidered entirely to avoid manipulation and guiding problems. The guiding and centering function of the rotor has to be fulfilled on the stator chip with interfaces to the macro world.

The development of a new rotor with vertical legs, fabricated with microtechnologies, resulted in a more efficient behavior and higher dimensional reproducibility. The characterization of this new rotor was performed with a non-microfabricated stator membrane, consisting of a commercially available bulk PXE PZT piezoelectric disk glued onto a chemically etched copper beryllium membrane. The maximal measured torque of the new rotor was 2.7 µNm, corresponding to a speed of 25 rad/s. This values correspond to an increase of 20 to 30%, speed and torque characteristics, compared to the previous rotor fabricated with standard technologies.

The development of this new rotor design also stimulated the development of new technologies based on high-aspect ratio structuring of commercially available positive photoresists and followed by nickel electroplating, with conventional photolithographic tools. The optimized processes have proven to be very reproducible and allow the fabrication of 38 µm and 85 µm thick photoresist molds with a yield close to 100%. Spin coating sequences have been developed to minimize the edge-bead width and to obtain a layer thickness uniformity of 5%. A single exposure step was performed for both the 38 µm and 85 µm thick layer processes. The fabricated photoresist molds have demonstrated to be fully compatible with nickel electroplating. The combination of the thick positive resist process with photostructuration of the epoxy-based SU-8 resist opens the way to low cost fabrication of complex metallic and plastic structures for MEMS applications use.

Appendix A. The compliance and rigidity matrix in details

A.1. Cantilevers flexion theory

A.1.1. Force applied to a cantilever

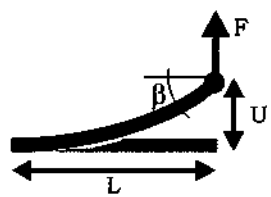

$$\text{bending} : U = \frac{F \cdot L^3}{3EI} \tag{1}$$

$$\text{angle} : \beta = \frac{F \cdot L^2}{2EI} \tag{2}$$

Where:
- F: Applied force
- L: Cantilever length
- E: Young modulus
- I: Moment of inertia (defined bellow (5))

A.1.2. Momentum applied to a cantilever

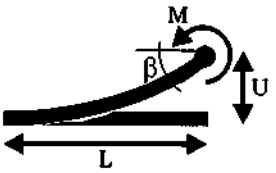

$$\text{bending} : U = \frac{M \cdot L^2}{2EI} \tag{3}$$

$$\text{angle} : \beta = \frac{M \cdot L}{EI} \tag{4}$$

Where: M: Applied momentum

A.1.3. Inertia momentum

The inertia momentum of a rectangular shape structure is given by:

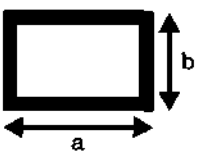

$$\text{Inertia momentum} : I = \frac{a\,b^3}{12} \tag{5}$$

Where: a: beam length

b: beam thickness

A.2. Decomposition of forces and deformations in x et y

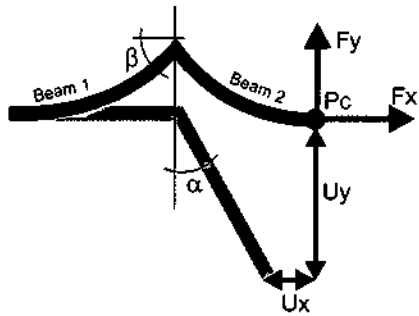

Where: Fx: Force in x

Fy: Force applied in y

Ux: Deformation in x

Uy: Deformation in y

A.2.1. Deformation of beam 1

A.2.1.1 Force applied in the direction x → Fx

Characterization of the displacement of the point Pc when a force Fx is applied. The beam 2 is unbuckled.

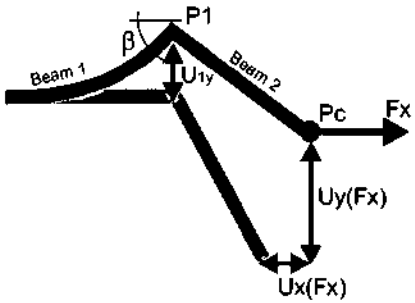

The displacement of the point Pc is due to the displacement of the point P1 and the angle β.

Point P1 displacement due to momentum M ($M = Fx\ L_2 \cos(\alpha)$) Equ. (3)

$$U_{1x}(Fx) = 0$$

$$U_{1y}(Fx) = \frac{Fx\ L_1^2\ L_2 \cos(\alpha)}{2EI}$$

Angle due to momentum M Equ. (4)

$$\beta(Fx) = \frac{Fx\ L_1\ L_2 \cos(\alpha)}{EI}$$

Point Pc displacement due to the angle β(Fx)

$$U_{\beta x}(Fx) = \beta(Fx)\ L_2 \cos(\alpha) = \frac{Fx\ L_1\ L_2^2 \cos^2(\alpha)}{EI}$$

$$U_{\beta y}(Fx) = \beta(Fx)\ L_2 \sin(\alpha) = \frac{Fx\ L_1\ L_2^2 \cos(\alpha)\sin(\alpha)}{EI}$$

The displacement of the point Pc, due to the force Fx, is the sum of the displacement of the point P1 and Pc due to the angle β.

$$U_x(Fx) = U_{1x}(Fx) + U_{fix}(Fx) = 0 + \frac{Fx\, L_1\, L_2^2 \cos^2(\alpha)}{EI}$$

$$U_y(Fx) = U_{1y}(Fx) + U_{fiy}(Fx) = \frac{Fx\, L_1^2\, L_2 \cos(\alpha)}{2EI} + \frac{Fx\, L_1\, L_2^2 \cos(\alpha)\sin(\alpha)}{EI}$$

A.2.1.2 Force applied in the direction y → Fy

Characterization of the displacement of the point P1 when a force Fy is applied at the point Pc. The beam 2 is unbuckled.

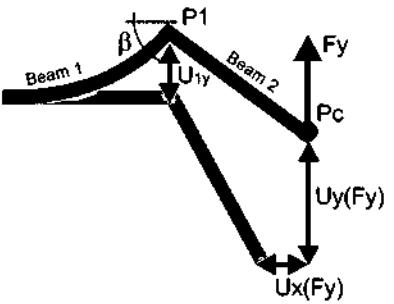

Point P1 displacement due to momentum M =Fy sin(α)L_2 Equ. (3)

$$U_{1x,M}(Fy) = 0$$

$$U_{1y,M}(Fy) = \frac{Fy\, L_1^2\, L_2 \sin(\alpha)}{2EI}$$

Point P1 displacement due to the force Fy Equ. (1)

$$U_{1x}(Fy) = 0$$

$$U_{1y}(Fy) = \frac{Fy\, L_1^3}{3EI}$$

Angle due to the momentum M Equ. (4)

$$\beta(Fy) = \frac{L_2 \sin(\alpha)\, Fy\, L_1}{EI}$$

Angle due to the force Fy Equ. (2)

$$\beta(Fy) = \frac{Fy\, L_1^2}{2EI}$$

Point Pc displacement due to β(Fy)

$$U_{\beta c}(Fx) = \beta(Fy)\, L_2 \cos(\alpha) = \left(\frac{Fy\, L_1\, L_2 \sin(\alpha)}{EI} + \frac{Fy\, L_1^2}{2EI}\right) L_2 \cos(\alpha)$$

$$U_{\beta c}(Fx) = \beta(Fy)\, L_2 \sin(\alpha) = \left(\frac{Fy\, L_1\, L_2 \sin(\alpha)}{EI} + \frac{Fy\, L_1^2}{2EI}\right) L_2 \sin(\alpha)$$

The displacement of the point Pc, due to the force Fy, is the sum of the displacement of the point P1 and Pc due to the angle β.

$$U_x(Fy) = U_{1x,M}(Fy) + U_{1x}(Fy) + U_{\beta c}(Fy)$$

$$U_x(Fy) = 0 + \left(\frac{Fy\, L_1\, L_2 \sin(\alpha)}{EI} + \frac{Fy\, L_1^2}{2EI}\right) L_2 \cos(\alpha)$$

$$U_y(Fy) = U_{1y,M}(Fy) + U_{1y}(Fy) + U_{\beta y}(Fy)$$

$$U_y(Fy) = \frac{Fy\, L_1^2\, L_2 \sin(\alpha)}{2EI} + \frac{Fy\, L_1^3}{3EI} + \left(\frac{Fy\, L_1\, L_2 \sin(\alpha)}{EI} + \frac{Fy\, L_1^2}{2EI}\right) L_2 \sin(\alpha)$$

A.2.2. Compliance matrix C_1 of beam 1

The compliance matrix coefficients are obtained by dividing calculated deformations by the corresponding force.

$$\begin{pmatrix} Ux \\ Uy \end{pmatrix} = \underbrace{\begin{pmatrix} C1xx & C1xy \\ C1yx & C1yy \end{pmatrix}}_{C_1} \begin{pmatrix} Fx \\ Fy \end{pmatrix} \qquad C1xx = \frac{Ux(Fx)}{Fx} \qquad C1xy = \frac{Ux(Fy)}{Fy}$$

$$C1yx = \frac{Uy(Fx)}{Fx} \qquad C1yy = \frac{Uy(Fy)}{Fy}$$

$$C1xx = \frac{U_y(Fx)}{Fx} = \frac{L_1 L_2^2 \cos^2(\alpha)}{EI}$$

$$C1xy = \frac{U_y(Fy)}{Fy} = \left(\frac{L_1 L_2 \sin(\alpha)}{EI} + \frac{L_1^2}{2EI} \right) L_2 \cos(\alpha)$$

$$C1yx = \frac{U_y(Fx)}{Fx} = \frac{L_1^2 L_2 \cos(\alpha)}{2EI} + \frac{L_1 L_2^2 \cos(\alpha)\sin(\alpha)}{EI}$$

$$C1yy = \frac{U_y(Fy)}{Fy} = \frac{L_1^2 L_2 \sin(\alpha)}{2EI} + \frac{L_1^3}{3EI} + \left(\frac{L_1 L_2 \sin(\alpha)}{EI} + \frac{L_1^2}{2EI} \right) L_2 \sin(\alpha)$$

A.2.3. Deformation of beam 2

A.2.3.1 Force applied in the direction x → Fx

Characterization of the displacement of the point Pc when a force Fx is applied at the point Pc. The beam 1 is unbuckled.

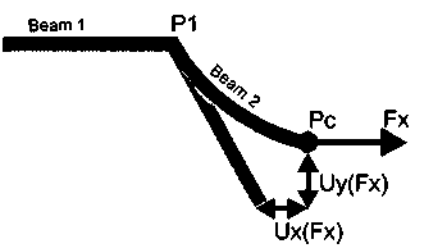

Point Pc displacement due to the force Equ. (1)

$$U_x(Fx) = \frac{Fx\, L_2^3 \cos^2(\alpha)}{3EI}$$
$$U_y(Fx) = \frac{Fx\, L_2^3 \cos(\alpha)\sin(\alpha)}{3EI}$$

A.2.3.2 Force applied in the direction y → Fy

Characterization of the displacement of the point Pc when a force Fy is applied at the point Pc. The beam 1 is unbuckled.

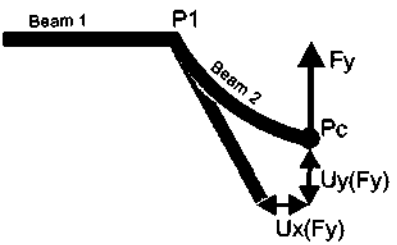

Point Pc displacement due to the force Fy Equ. (1)

$$U_x(Fy) = \frac{Fy\, L_2^3 \cos(\alpha)\sin(\alpha)}{3EI}$$
$$U_y(Fy) = \frac{Fy\, L_2^3 \sin^2(\alpha)}{3EI}$$

A.2.4. Compliance matrix C_2 of beam 2

The compliance matrix coefficients are obtained by dividing calculated deformations by the corresponding force.

$$C2xx = \frac{U_x(Fx)}{Fx} = \frac{L_2^3 \cos^2(\alpha)}{3EI}$$

$$C2xy = \frac{U_x(Fy)}{Fy} = \frac{L_2^3 \cos(\alpha)\sin(\alpha)}{3EI}$$

$$C2yx = \frac{U_y(Fx)}{Fx} = \frac{L_2^3 \cos(\alpha)\sin(\alpha)}{3EI}$$

$$C2yy = \frac{U_y(Fy)}{Fy} = \frac{L_2^3 \sin^2(\alpha)}{3EI}$$

A.3. MATLAB program to calculate the K matrix

These Matlab programs calculate the matrix of rigidity for the CuBe and the vertical legs rotors.

A.3.1. Function calculating the compliance matrix

A.3.1.1 Function calculating the matrix C of beam 1

Compl_p1.m:

```
function C_mat=compl_p1(lone,ltwo,alpha);

%this function calculates the compliances for "beam one"
%to get final values the matrix has to be divlde by E*I.

C_mat=zeros(2,2);

C_mat(1,1)=(ltwo*cos(alpha))^2*lone;
C_mat(1,2)=(ltwo*cos(alpha))*(0.5*lone^2+ltwo*lone*sin(alpha));

C_mat(2,1)=ltwo^2*lone*sin(alpha)*cos(alpha) +0.5*ltwo*cos(alpha)*lone^2;
C_mat(2,2)=lone^3/3+(lone^2*ltwo*sin(alpha)*0.5);
C_mat(2,2)=C_mat(2,2)+(0.5*lone^2+ltwo*lone*sin(alpha))*ltwo*sin(alpha);
```

A.3.1.2 Function calculating the matrix C of beam 2

Compl_p2.m:

```
function C_mat=compl_p2(lone,ltwo,alpha);

%this function calculates the compliances for "beam two"
%to get final values the matrix has to be divide by E*I.

C_mat=zeros(2,2);

C_mat(1,1)=cos(alpha)^2;
C_mat(1,2)=cos(alpha)*sin(alpha);

C_mat(2,1)=cos(alpha)*sin(alpha);
C_mat(2,2)=sin(alpha)^2;
C_mat=C_mat*ltwo^3/3;
```

A.3.2. The rigidity matrix of the CuBe rotor

```
%*-------------------------------------------------
%*Rigidity matrix of the CuBe rotor
%*-------------------------------------------------

clear all

epaisseur=30e-6;
E=105e9;                                %Module de Young of Ni
largeur=120e-6;
ltwo=220e-6;
lone=60e-6;
alpha=17;
alpha=alpha*pi/180;

%Definitions
I=largeur*epaisseur^3/12;               %Moment of inertia
EI=E*I;


%Program



cone=compl_p1(lone,ltwo,alpha);         % function compl_p1

ctwo=compl_p2(lone,ltwo,alpha);         % function compl_p2

K=EI*inv(cone+ctwo);


K_Fx_y=abs(K(1,2));
K_Fy_y=abs(K(2,2));

K                                       %print matrix K
```

A.3.3. Matlab program to calculate de dimensioning of the vertical legs rotor

```
%*-------------------------------------------------
%*Rigidity matrix of the Ni vertical legs rotor
%*-------------------------------------------------


clear all                               %Initialization of variables

%Constants

E=210e9;                                % Young Modulus of Ni
epaisseur_CuBe=30e-6;
largeur=120e-6;                         %widht=80e-6 et 50e-6
L1_max=150e-6;
LI_min=10e-6;
L2_max=250e-6;
```

```
L2_min=20e-6;
number=50;                                  %Nb de pts calculated
alpha=7*pi/180;
epaisseur=24e-6;

%Definitions
I=largaur*epaisseur^3/12;                   %Moment of inertia
EI=E*I;

%Program

for J = 1:number,

ltwo=(L2_max-L2_min)/(number-1)*(J-1)+L2_min;  %H

for N = 1:number,

lone=(L1_max-L1_min)/(number-1)*(N-1)+L1_min;          %L

cone=compl_p1(lone,ltwo,alpha);
ctwo=compl_p2(lone,ltwo,alpha);

K=EI*inv(cone+0*ctwo);              %Beam 2 not buckled

%Preparation of the exportation matrix

%K_Fx_y(N)=abs(K(1,2));
%K_Fy_y(N)=abs(K(2,2));

K_Kxy(N+1,1)=lone;
K_Kyy(N+1,1)=lone;
K_Kxy(N+1,J+1)=abs(K(1,2));
K_Kyy(N+1,J+1)=abs(K(2,2));

end
K_Kxy(1,J+1)=ltwo;
K_Kyy(1,J+1)=ltwo;

end

save c:\ikxy.txt K_Kxy /ascii
save c:\ lkyy.txt K_Kyy /ascii
```

Acknowledgments

Thank you, Professor Nico de Rooij for giving me the opportunity to work in your group from 1996 to 2000! During these four years I discovered the fascinating world of microfabrication in a very stimulating environment. Thank you also for your support during all the time of this project and for your encouragement to present this work at different international congresses.

I would particularly thank Dr. Georges-André Racine who was my project leader, for introducing and guiding me in the capricious piezoelectric technology, for accepting to be one of the co-examiner of my thesis, and for his comments and suggestions during these four years.

Special thanks to Prof. Dr. Heinz Hügli from University of Neuchâtel and Dr. Roland Luthier from the Swiss Federal Institute of Technology Lausanne, for kindly agreeing to be examiners of this thesis.

The realization of this work would not have been possible without the competence of our technicians. Thank you! Sylvain Jeanneret for managing the lab and providing us very powerful equipment, Gianni Mondin for your caustic comments and useful suggestions, Sylviane Pochon for all dicings and wire bondings, José Vaquera and Sabina Jenny for your support. Special thanks to Pierre-André Clerc for all winter Monday snow reports and for his precious tips about... amazing free ride spots around Verbier! More seriously, thank you Clairon for your flexibility, suggestions, and numerous trials for the development of the nickel electroplating into photoresist molds and deep reactive ion etching processes.

I am grateful to Professor Milena Koudelka-Hep and Dr. Peter Van der Wal who explained me some mysteries of the chemistry, Dr. Philippe Luginbühl for his help with piezoelectric layers, and for animated and instructive discussions, Dr. "Nose" Marco Meijerink for helping me with Labview and Benedikt Guldimann, for explaining me some of the fiber optic mysteries and for showing me what working (too) hard means...

My gratitude also goes to Dr. Sabeth Verpoorte for spending hours on this manuscript to correct my "Frenglish" and for giving helpful suggestions about positive photoresist theory.

Thanks also to Dr. Cynthia Beuret for introducing me in the microfabrication laboratory during my diploma work and for giving me useful advice for the positive resist process development, and to Sebastien Gautsch who made a very nice work during his diploma project, by developing an assembly clipping technique, based on nickel electroplating.

A special thank to Dr. Hubert Lorenz from EPFL for his helpful collaboration on the SU-8 process development and Jacky Labourey, from our industrial partner ASULAB SA / SwatchGroup, for the development of different prototypes.

Thank you, Dr. PFI-Honoré Désiré (P.-F. Indermühle) for your collaboration on different projects and specially for your support from the sunny beach, when we were in the lab, working for you...

Last but not least, thank you to co-founders of the non profit organization KTS, Bastien Droz, Dr. PFI, Sylvain Roth, Gregor Schürmann, and a dissident, Danick Briand, for all "social" activities and events organized inside and outside of the IMT group.

List of publications

Refereed articles

- S. Roth, L. Dellmann, G.-A. Racine, N.F. de Rooij, "High aspect ratio UV photolithography for electroplated structures", Journal Micromechanical Microengineering, vol. 9, pp. 105-108, 1999.
- L. Dellmann, S. Roth, C. Beuret, G.-A. Racine, H. Lorenz, M. Depont, P. Renaud, P. Vettiger, N. F. de Rooij, "Fabrication process of high aspect ratio elastic and SU-8 structures for piezoelectric motor applications", Sensors and Actuators, A Physical, vol. 70, pp. 42-47, 1998.
- L. Dellmann, S. Roth, C. Beuret, L. Paratte, G.-A. Racine, H. Lorenz, M. Despont, P. Renaud, P. Vettiger, N. F. de Rooij, "Two steps micromoulding and photopolymer high-aspect ratio structuring for applications in piezoelectric motor components", Microsystem Technologies, vol. 4, no. 3, pp. 147-150, 1998.
- P.-F. Indermuhle, S. Roth, L. Dellmann, N.F. de Rooij, "Patterned thick photoresist layers for protection of protruding structures during wet and dry etching processes", Journal of Micromechanics and Microengineering, vol. 8, no. 2, pp. 74-76, 1998.
- P.-A. Clerc, L. Dellmann, F. Grétillat, M.-A. Grétillat, P.-F. Indermühle, S. Jeanneret, Ph. Luginbubl, C. Marxer, T.L. Pfeffer, G.-A. Racine, S. Roth, U. Staufer, C. Stebler, P. Thiébaud, N.F. de Rooij, "Advanced deep reactive ion etching: a versatile tool for micromechanical systems", Journal of Micromechanics and Microengineering, vol. 8, pp. 272-278, 1998.

Conference proceedings

- L. Dellmann, G.-A. Racine, N.F. de Rooij, "Micromachined piezoelectric elastic force motor", Proc. IEEE Micro Electro Mechanical Systems - MEMS '00, Miyazaki, Japan, p. 52-55, 2000.
- L. Dellmann, S. Gautsch, G.-A. Racine, N. F. de Rooij, "New integrated axle fabrication for piezoelectric motors based on a rotor clip assembling operation", Digest of Technical Papers 10th Internat. Conf. on Solid-State Sensors and Actuators, TRANSDUCERS '99, Sendai, J, pp. 1752-1755, 1999.
- S. Roth, L. Dellmann, G.-A. Racine, N.F. de Rooij, "High aspect ratio UV photolithography for electroplated structures", Proc. Micromechanics Europe '98, Ulvik, N, pp. 55-58, 1998.
- L. Dellmann, S. Roth, C. Beuret, G.-A. Racine, H. Lorenz, M. Despont, P. Renaud, P. Vettiger, N.F. de Rooij, "Fabrication Process of High Aspect Ratio Elastic Structures for Piezoelectric Motor Applications", Digest of Technical Papers of the 9th Internat. Conf. on Solid-State Sensors & Actuators, TRANSDUCERS '97, Chicago, USA, pp. 641-644, 1997.
- P.-F. Indermuhle, L. Dellmann, S. Roth et N.F. de Rooij, "Patterned Thick Photoresist Layers for Protection of Protruding Structures During Wet and Dry Etching Processes", Proc. Micromechanics Europe '97, Southampton, UK, pp. 39-42, 1997.